Modelling Light Scattering in the Human Retina

Ana Sílvia F. C. Silva
University of Coimbra
Department of Physics
Under the supervision of
Adérito Araújo, Ph.D.
Sílvia Barbeiro, Ph.D.

Ana Sílvia Ferreira Diamantino Coelho e Silva

MODELLING LIGHT SCATTERING IN THE HUMAN RETINA

DEPARTMENT OF PHYSICS
UNIVERSITY OF COIMBRA
2013

Dissertação apresentada à Faculdade de Ciências e Tecnologia da Universidade de Coimbra, para a obtenção do Grau de Mestre em Engenharia Biomédica.

Trabalho desenvolvido no âmbito do projecto de investigação PTDC/SAU-ENB/119132/2010.

Agradecimentos

Antes de a qualquer outra pessoa, queria aqui expressar o meu agradecimento ao Prof. Adérito Araújo e à Profª Sílvia Barbeiro, que me apoiaram ao longo do ano e me ajudaram a ambientar-me a um tipo de trabalho com o qual não estava de todo familiarizada. Este agradecimento estende-se a todo o grupo de investigação, em especial ao Prof. Miguel Morgado e ao Prof. Rui Bernardes, pela disponibilidade apresentada para esclarecimento de dúvidas e fornecimento de bibliografia essencial à realização deste trabalho.

Deixo também, a um nível mais pessoal, um agradecimento à família, em especial à mãe, ao pai e ao irmão. Aos amigos novos e velhos, pela companhia, e um agradecimento especial ao namorado, por todo o apoio e paciência ao longo deste ano.

Muito obrigada.

Abstract

Abstract

Medical imaging techniques are a major application of many of the scientific findings of the past decades. The interest in these applications is obvious, since better imaging techniques can both improve the quality of diagnostics and allow for better understanding of natural phenomena. One of the most recent innovations in *in vivo*, non-invasive imaging is Optical Coherence Tomography. The main use of this technique in medical imaging is to acquire high resolution, tri-dimensional images of the eye fundus, allowing for detailed anatomical characterisation of the retina [5, 14].

The retina is nervous tissue in the eye and the most important component in our sense of vision. There are many diseases that affect the eye, and whose diagnosis isn't straightforward. The sensitivity of this structure makes medical analysis quite complicated. Most of the diagnoses are made either by direct observation, with the possible injection of dyes to enhance certain parts of the organ, or by numbing the eye and directly measuring its inner pressure or thickness. Optical coherence tomography, on the other hand, allows for imaging in the histological range without being invasive [7], which is an incredible improvement relative to the techniques above described. As it is relatively recent, there are still open possibilities for this technique — diagnosing different types of pathologies or acquiring functional information, for instance. In order to study these possibilities, a mathematical model was suggested. A mathematical model is an incredibly useful tool for exploring and better understanding many physical phenomena, without spending expensive physical resources.

Since we want to study the impact of the changes at cellular-level on the final image, our model must go back to the cellular-level interactions that culminate in the optical coherence tomography scan image. This means studying light propagation and diffraction in a heterogeneous medium. To reach this goal, we will study the fundamentals of electromagnetism and use their foundations – Maxwell's equations – in order to model at a very small scale how an electromagnetic wave propagates [24].

The continuous theoretical model that is considered is complemented with a discrete model, built using finite differences and considering appropriate boundary and initial conditions. The numerical results obtained show the potential this approach has. The study presented on this work gave origin to two scientific works [3, 24]

Keywords: Maxwell Equations, Optical Coherence Tomography, Finite Differences, Retina, Light Scattering

Resumo

A imagiologia médica é uma das principais aplicações de muitas das inovações científicas das últimas décadas. O interesse no desenvolvimento desta área é óbvio, visto que melhores técnicas de imagiologia permitem melhorar a qualidade dos diagnósticos e a compreensão de fenómenos naturais. Uma das mais recentes inovações em imagiologia *in vivo* não invasiva é Tomografia de Coerência Óptica. A principal utilização desta técnica é para aquisição de imagens tridimensionais de alta definição do fundo do olho, permitindo uma caracterização anatómica da retina em grande detalhe [5, 14].

A retina é tecido nervoso no olho de extrema importância na nossa visão. Há muitas doenças que afectam o olho e cujo diagnóstico não é directo – a sensibilidade desta estrutura torna a análise médica complicada. A maior parte dos diagnósticos é feita ou por observação directa, com a possível injecção de contrastes que realcem partes do órgão, ou por entorpecimento do órgão e posteriores medições diretas de grandezas como a pressão interna ou a espessura. A tomografia de coerência óptica, por outro lado, permite a aquisição de imagens de qualidade histológica de forma não invasiva [7], o que é uma melhoria extrema em comparação com os métodos acima descritos. Visto ser uma técnica relativamente recente, há variadas possibilidades em aberto, nomeadamente o diagnóstico de outros tipos de patologias, ou a aquisição de informação funcional. O estabelecimento de um modelo matemático para a tomografia de coerência óptica revela-se de extrema importância pois permite explorar e compreender melhor os fenómenos físicos envolvidos no processo sem que para isso seja necessário recorrer a experiências físicas dispendiosas.

Nesta dissertação pretendemos estudar o efeito que as alterações ao nível celular provocam na imagem final. O modelo matemático a considerar deve, por isso, descrever as interacções que ocorrem a essa escala e que eventualmente levam à imagem de tomografia de coerência óptica. Isto implica estudar a propagação e difracção da luz num meio heterogéneo. Nesse sentido, vamos estudar os fundamentos de electromagnetismo e usar as equações de Maxwell para modelar a uma escala muito pequena a maneira como uma onda electromagnética se propaga.

O modelo teórico contínuo considerado é complementado com um modelo discreto construído com recurso ao método das diferenças finitas onde foram consideradas condições iniciais e de fronteira adequadas. Os resultados numéricos obtidos evidenciam as potencialidades desta abordagem. O estudo apresentado nesta dissertação deu origem a dois trabalhos científicos [3, 24].

Palavras chave: Equações de Maxwell, Tomografia de Coerência Óptica, Diferenças finitas, Retina, Dispersão da Luz

Contents

Abbreviations

ABC	Absorbing Boundary Condition
ADI-FDTD	Alternating-Direction Implicit Finite-Difference Time-Domain
AMD	Age-related Macular Degeneration
CME	Cystoid Macular Edema
DME	Diabetic Macular Edema
DR	Diabetic Retinopathy
ELM	External Limiting Membrane
FDTD	Finite-Difference Time-Domain
GCL	Ganglion Cell Layer
ILM	Inner Limiting Membrane
INL	Inner Nuclear Layer
IPL	Inner Plexiform Layer
LCI	Low Coherence Interferometry
NFL	Nerve Fibre Layer
OCT	Optical Coherence Tomography
ONL	Outer Nuclear Layer
OPL	Outer Plexiform Layer

PL	Photoreceptor Layer
PML	Perfectly Matched Layer
RPE	Retinal Pigment Epithlium
TD-OCT	Time-Domain Optical Coherence Tomography
TE	Transverse Electric
TM	Transverse Magnetic

List of Figures

Chapter 1

Introduction

To better understand some of the problems faced when working towards a mathematical model to describe light scattering in the human retina, we find it important to explain, with some degree of detail, the anatomy of the human eye. Greater focus will be given to the cellular components of the retina, and how these parts work together allowing us to see. We will also identify certain pathologies that are relatively common and how they relate to cellular alterations of the retinal tissue. We will also explain the processes that lead to an optical coherence tomography image.

1.1 The Eye and the Retina

The human eye is a complex structure, vital regarding our sense of vision. A scheme of its basic structure can be seen on Figure 1.1. As light enters the eye, it is focused by the cornea. The iris adjusts its size in order to select the "amount" of light that passes through the pupil; the crystalline further focuses this light beam, which then converges on the retina [18].

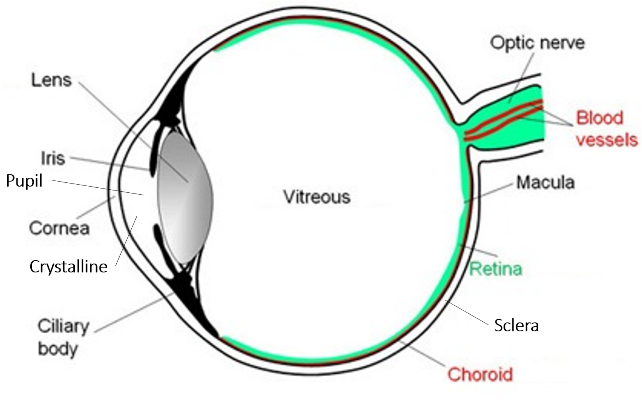

Figure 1.1: Scheme of the eye.

The retina is one of the three layers that lines the inside of the eye. The outermost one is the sclera that includes the cornea and is responsible for the organ's protection; the middle layer is the choroid, which is a vascular layer, responsible for oxygenation and nourishment of the retina – the innermost layer, and the one of more interest regarding the sense of vision [20].

The retina is considered part of the central nervous system, as during embryonic development it originates as an outgrowth of the brain [19]. Anatomically, it can be split into distinct layers, as seen on Figure 1.2.

The most internal layer is the inner limiting membrane, ILM. It is the boundary between the retina and the vitreous body (a clear gel that fills the space between the lens and the retina), constituted by astrocytes and by the feet of Müller cells – glial cells that serve as support for the neurons in the retina. Between this layer and the next – the nerve fibre layer, NFL – there is a thin layer of Müller cells' footplates. At the NFL are the axons of the ganglion cells (that will form the optic nerve), which are neurons whose nuclei are in the following layer, appropriately named ganglion cell layer, GCL. The next layer is where the synapses between the dendrites of the gan-

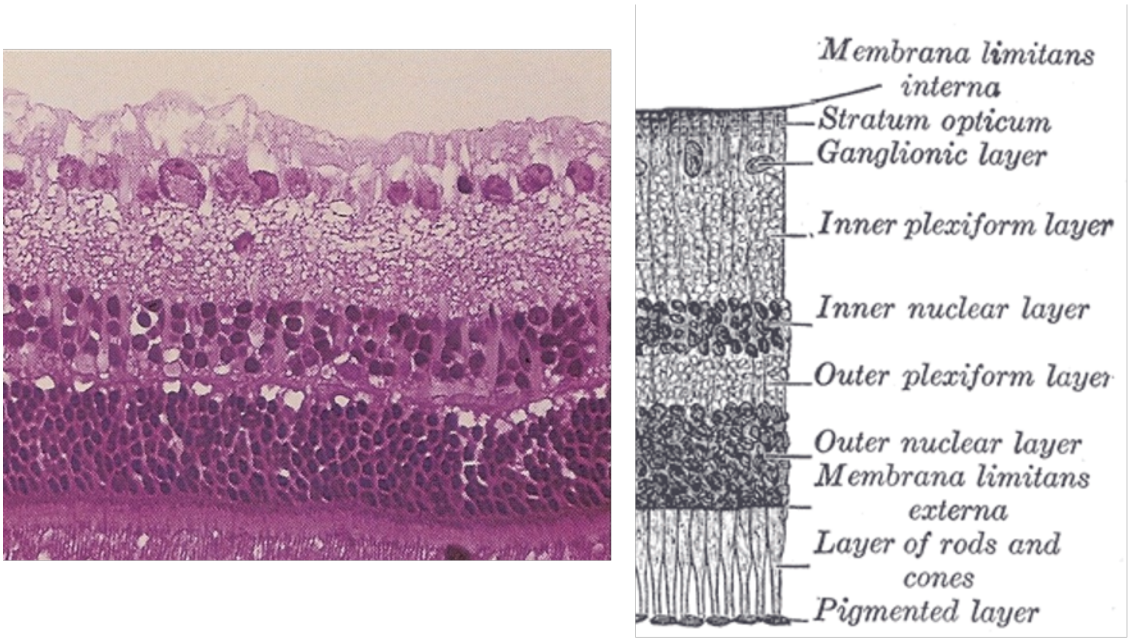

(a) *(b)*

Figure 1.2: (*a*) Histological image of the retina [20]; (*b*) Scheme of the layers.

glion cells and the axons of the bipolar neurons occur, in a dense reticulum of fibrils – the inner plexiform layer, IPL. Past this layer is the inner nuclear layer, INL, where the nuclei of the bipolar neurons are located (and some amacrine cells, which are interneurons). After this layer is the outer plexiform layer, OPL. Here is where the synapses between the photosensitive cells' axons and the bipolar neurons' dendrites occur. Projections of the photosensitive cells (spherules for the cones, pedicles for the rods) are in this layer; its cell bodies are in the following layer, the outer nuclear layer, ONL. After the ONL there is a membrane, the external limiting membrane, ELM, which separates the rods' and cones' nuclei from their outer segments, which are located in the photoreceptor layer, PL. It is the outer segments of these cells that are photosensitive and initiate the events that culminate in the formation of an image. The cones are sensitive to three wavelength bands, corresponding to three colors: red (long cones), green (medium cones) and blue (short cones). They are abundant in the foveal region. The fovea is a part of the retina, responsible for sharp, central vision, that is located in the macula – which in turn is an oval-shaped, highly pigmented spot near the center of the retina. Rods are more common in the peripheral regions of the eye, and are especially important in low-light vision. The final layer is a single layer of cuboidal epithelial cells, the retinal pigment epithelium, RPE, which is attached to the choroid [19, 20].

As light enters the eye, it is refracted, as it passes through the cornea and again through the lens. These refractions result on the projection of an inverted image on the retina, a result identical to the refractions that occur when a biconvex lens is employed. In the retina, proteins that exist on the photoreceptors, called opsines, absorb a photon and initiate a transduction pathway that culminates in the hyper-polarization of the cell. The cells then synapse with the bipolar neurons, which in turn synapse with the ganglion cells. From there, the information is lead to the brain through the optic nerve. There are approximately 130 million photoreceptors to 1.2 million ganglion cells (10% of which are in the foveal region); this is because the information is processed in the course of the synapses previously described.

As one can see, the retina is an intricate structure with many different cells, all responsible for different parts in the sensory response to light. There are a number of pathologies that affect the retina (and therefore one's vision) that trace back to cellular damages in one or more of the above specified layers. Common examples of these pathologies are macular edema, diabetic retinopathy, glaucoma and macular degeneration.

Macular edema occurs when there is some kind of lesion that causes fluids and proteins to accumulate in the macula. It is a common condition following cataract surgery. This pathology can be classified as cystoid macular edema (CME), which involves fluid accumulation in the OPL consequent of abnormal permeability of the capillaries in the perifovea (it should be noted that despite its name, this edema isn't cystic, as it has no epithelial coating – it's its appearance that gives it such a name). Another type of macular edema is the diabetic macular edema, DME, which is similarly caused by leaking from macular capillaries, usually consequent of diabetic retinopathy – and the most common cause for vision loss in patients who have that condition. It is estimated that 45% of diabetics will develop DME at some stage of their lives[1].

Diabetic retinopathy, DR, refers to retinal damages following diabetes. It affects nearly 80% of all patients that have had diabetes for more than 3 years, and is a leading cause of blindness in american adults[2]. DR is the result of micro-vascular changes; the inadequate concentrations of glucose in the blood plasma lead to alterations in the blood-retinal barrier and to an increased permeability of the retinal blood vessels. Accumulation of glucose and/or fructose damages the small blood vessels. If not addressed, as it progresses the disease enters a different stage: proliferative DR. The damage to the blood vessels causes low oxygenation, which is a trigger for the start of angiogenesis (the formation of new blood vessels). These new blood vessels can grow along the retina and in the vitreous humour; due to their frailty, they can easily bleed and cloud one's vision, cause retinal detachment (where the eye "peels" from its underlying support tissue, the sclera) or even lead to glaucoma.

Glaucoma is a disease in which the optic nerve is damaged in a certain pattern, possibly leading to blindness. It is usually a consequence of increased pressure in the aqueous humour, a gelatinous

---

[1] Statistics from http://www.virtualmedicalcentre.com/diseases/diabetic-macular-oedema, accessed on June 15th, 2013.

[2] Statistics from the National Eye Institute, http://www.nei.nih.gov/eyedata/diabetic.asp, accessed on June 15th, 2013.

fluid located in the space between the lens and the cornea (not to be confused with vitreous humour). The nerve damage is due to loss of ganglion cells. It is estimated that over 2.2 million americans have glaucoma, but only half of these are aware[3].

Macular degeneration is a condition related to age (in fact, usually called age-related macular degeneration, AMD) that results in loss of vision due to retinal damage in the macula. There are two forms of this disease: "dry" AMD and "wet" AMD. The first results from atrophy of the cells of the RPE and consequent loss of rods and cones; the second causes vision loss due to abnormal blood vessel growth that ultimately leads to leakage of blood and proteins below the macula. Such aggressions lead to irreversible damage to the photoreceptors. This disease is another of the leading causes for vision loss[4].

These pathologies can all be identified by anatomical analysis of the retina. Its dimensions, however, are quite small; the retina's thickness varies between 0.10 mm on its outer parts to 0.24 mm in the perifoveal region, and again 0.10 mm in the fovea, [19], as seen on Figure 1.3. These dimensions imply that to obtain an accurate portrait of the retina, a high-resolution technique must be employed.

---

[3] Statistics from http://www.glaucoma.org/, accessed on June 15th, 2013.

[4] Statistics from the National Eye Institute, http://www.nei.nih.gov/eyedata/amd.asp, accessed on June 15th, 2013.

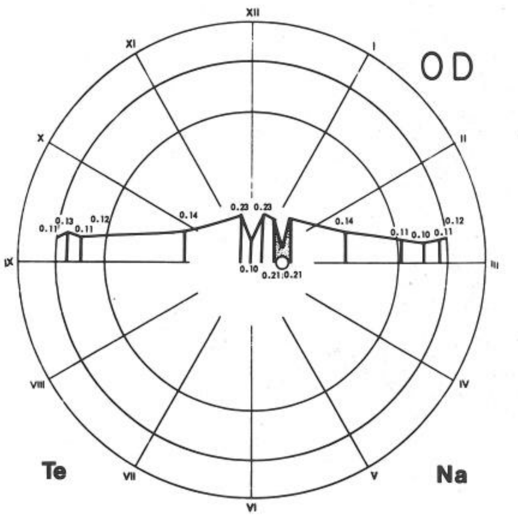

Figure 1.3: Representation of the thickness of the retina, from the temple (Te) to the nasal (Na) region, in milimeters [19].

1.2 Optical Coherence Tomography

Optical Coherence Tomography, OCT is a recent imaging technique that is highly advantageous for imaging the eye due to its high resolution. With it, we can obtain a tri-dimensional map of the eye fundus with a high level of detail, which is very useful and important for early diagnosis of pathologies as the ones described in the previous section. Besides this, it has the great advantage of being a non-invasive technique, which makes it a lot more comfortable for the patients and of easier access.

OCT is analogous to ultrasound imaging, but using light instead of sound [14]. In ultrasound imaging, an ultrasound pulse is sent to an area of interest. Sound travels at different speeds in different materials, and as it travels from one type of material to another, part is reflected back and part continues to travel forward. The portion that is reflected back is detected; the echo time delay and intensity of this signal are used in order to characterise the material that caused the reflection. The same principle is applied to electromagnetic waves;

however, since the speed of light is at least 10^6 times that of sound, direct measure of the echo time delays, which are in a very small scale, isn't possible with today's technology [6]. In order to bypass this obstacle and acquire this information, more sophisticated methods are necessary. In OCT, the method used is interferometry.

An electromagnetic beam can be characterised by its coherence. A coherent beam is one which is highly self-correlated; correlation is a value that quantifies the ability to predict the value of a certain property of the wave – be it intensity, frequency, or any other characteristic value – by knowing the values the wave previously took [13]. A low coherence electromagnetic beam (i.e. one that is self-correlated in a small space interval) is used in low coherence interferometry, LCI. This beam is emitted by a source and travels until it reaches a beam splitter, where it is split in two identical parts. One of the resulting beams travels to a reference mirror, where it is reflected back; the other goes through a sample (the eye, in our case) and there it is reflected back by the eye's different structures. As these two beams reach the splitter again, they are recombined. This is the principle behind Michelson's interferometer, an experiment done by Michelson and Morley in 1887 [13]. Coherent light beams, when combined, interfere either constructively or destructively, resulting in an interference pattern. This mechanism will be described in better detail.

The beams used in an OCT apparatus have small coherence lengths, which means that constructive interference happens only when both beams have travelled the same optical path, which is the distance the beam travelled in a certain medium multiplied by the refractive index of that medium [14]. The result of this constructive interference is detected by the photodetector [5, 6]. If we change the position of the mirror, we change the optical path the reference beam travels, and therefore it will constructively interfere with a portion of the other beam that was reflected by the sample at a different depth (i.e.

that travelled the same optical length as the reference beam), which is the principle behind TD(time-domain)-OCT [5], as described by Figure 1.4. It is this mode that most interests us, and it's in it that our work will be based upon.

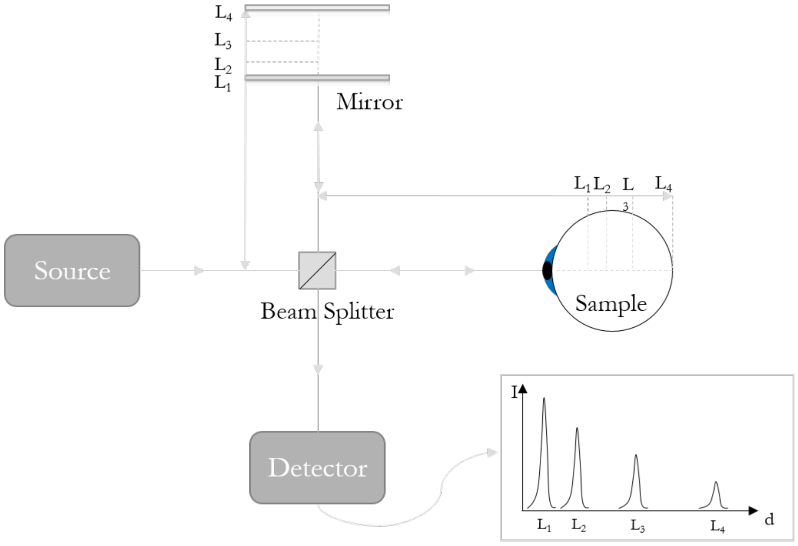

Figure 1.4: A scheme of time-domain OCT.

We can take different types of images from TD-OCT. When we change the position of the mirror, we get reflections from different depths for the same lateral position — an A-scan. If we take multiple A-scans along the same axis, all of them parallel between themselves, we have a bi-dimensional image of the retina — a B-scan. Multiple parallel B-scans make up a C-scan, a tri-dimensional map of the retina. Figure 1.5 represents these scans and how they relate to one another.

The intensity of the detected beam depends on the intensity of the reference beam and the structure's reflectivity. Different structures reflect the beam back in different proportions, and can therefore be identified by analysis of this signal.

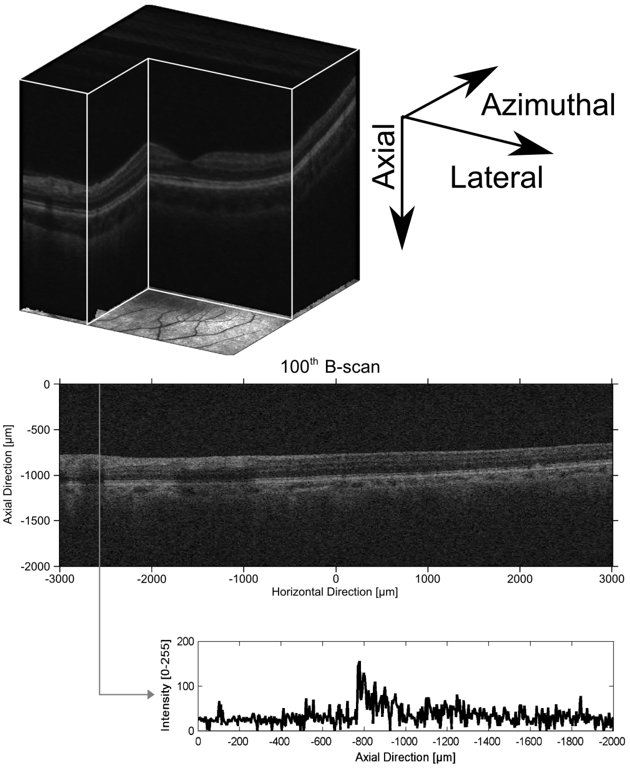

Figure 1.5: An OCT A-Scan, B-Scan and C-Scan of a human retina.

The axial resolution of an OCT scan is determined by the coherence length of the beam it uses. The transverse resolution is determined by the optics of the system and by the beams waist [12, 14].

OCT has many possible applications, even outside the clinical context (for instance, characterisation of materials [2]) [12]. However, its main application is in imaging the eye.

Chapter 2

Mathematical Model

2.1 State of the Art

The problem of light scattering in the human eye has been addressed in different ways by several research groups. Bulow *et al.* [8], in 1968, studied the scattering of light by the RPE granules, showing the existence of backscattering of light even when the pigment granules are inside the cells. Si *et al.* [23] modelled light scattering in retinal tissue using spherical and non-spherical models restricted to a cell, including the nucleous and other organelles. In 2001, Hammer *et al.* [16] determined absorption and scattering coefficients in the retina by modelling light transport in the retina, although not in a local scale. In 2007, Abdallah *et al.* [1] published a model for the study of photoreceptors. Although helpful toward developing what we're aiming for – that is, a model of light scattering in the whole retina – these works don't address many of the problems that concern us, specifically integrating the information necessary to produce an OCT scan in a model for light scattering.

We introduce this chapter to describe and explain the physical principles behind OCT. Besides, in order to have a model with the level of precision an OCT scan yields, we will need to go in detail into the electromagnetic processes that occur at cellular-level scale. To do so, we will use Maxwell's equations, the cornerstone of classical electromagnetism, to model light propagation and scattering in the retina.

2.2 Electromagnetism

Electromagnetism is the branch of physics that deals with the interactions between charged particles. The electromagnetic force is one of the four fundamental forces (alongside the weak and strong forces and the gravitational force), and it is responsible for almost all the phenomena encountered in one's daily life – with an exception for gravitational phenomena and nuclear scale events [13, 15].

In terms of nomenclature, there are a series of different names and symbols for a lot of the quantities we are going to deal with. With the goal of minimizing confusion, we attempt to describe the different fields in advance:

- $\vec{B}$, magnetic flux density;
- $\vec{H}$, magnetic field intensity;
- $\vec{D}$, electric flux density;
- $\vec{E}$, electric field intensity.

The flux densities and field intensities are related by the following equations:

$$\vec{B} = \vec{H} * \mu(\omega); \; \vec{D} = \vec{E} * \varepsilon(\omega).$$

In these equations, $*$ indicates convolution in time, μ the medium's magnetic permeability and ε the medium's electric permittivity, which in this case are dependent of the wave's frequency; if the medium is dispersionless (i.e., the permeability and permittivity are independent of the wave's frequency) the relations become $\vec{B} = \vec{H}\mu$; $\vec{D} = \vec{E}\varepsilon$.

The force an electromagnetic field exerts on a charged particle is characterized by Lorentz' law:

$$\vec{F} = q[\vec{E} + (\vec{v} \times \vec{B})], \tag{2.1}$$

where × denotes the vector cross product, $\vec{F}$ is the force, q is the particle's charge and $\vec{v}$ is the particle's instantaneous velocity, which is in vector form since it carries information regarding the direction of the particle's motion. The term $q\vec{E}$ is referenced as the electric force and $q(\vec{v} \times \vec{B})$ as the magnetic force.

There are two types of charges: negative, as in electrons, and positive, as in protons. Opposite charges are attracted towards one another, while equal ones repel each other. The interactions between charges are usually described in terms of electric fields, a concept which was introduced by Michael Faraday, who also determined the relationship between a changing magnetic field and an electric one [13, 15], and that will be detailed ahead. Electric fields are vector fields that describe the force exerted on a single positive charge. They are usually depicted as lines that leave positively charged particles (as they repel positive charges) and enter negatively charged particles (which attract positive charges). Similarly, a magnetic field is a vector field that mathematically describes the magnetic influence of electric currents and magnetic materials over charged particles. These two quantities are intimately related, and we usually talk about electromagnetic fields and the electromagnetic force. The relations between electric and magnetic fields are described further on.

The concept of electromagnetic fields can be expanded beyond the description of a force acting on a positively charged particle to a certain physical quantity that exists at a certain point of space (x, y, z) at a certain instant t, regardless there being any charged particle there at that time or not. We will then have two vectors, $\vec{E}$ (electric), with components E_x, E_y and E_z, which in turn vary with position and time – $E_x(x, y, z, t)$, $E_y(x, y, z, t)$, $E_z(x, y, z, t)$ – and $\vec{H}$ (magnetic), with components H_x, H_y, H_z that vary with position and time – $H_x(x, y, z, t)$, $H_y(x, y, z, t)$, $H_z(x, y, z, t)$.

2.3 Maxwell's Equations

The relations between charged particles and fields are comprised in a set of five equations — Lorentz' force law, (2.1), and Maxwell's four equations. Lorentz' law, (2.1), describes how the electromagnetic field influences a charged particle in its range; Maxwell's equations characterize how charged particles influence fields and how fields influence each other.

The first of these equations is Gauss's law for electric fields, and it describes the relationship between an electrically charged particle(s) and the electric field it creates:

$$\nabla \cdot \vec{E} = \frac{\rho}{\varepsilon_0}, \tag{2.2}$$

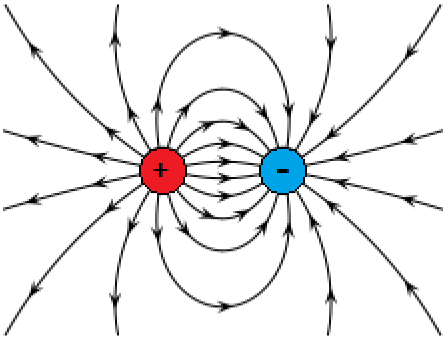

Figure 2.1: Electric field lines, entering a negative charge and leaving a positive one.

where ρ is the electric charge density, ε_0 is the vacuum permittivity and "$\nabla\cdot$" denotes the divergence operator. From this we understand that positively charged particles are sources of electric field lines and negatively charged ones are sinks for these same lines, as seen on Figure 2.1. Gauss's law for magnetic fields eliminates the possibility of any analogous particle for the magnetic case:

$$\nabla \cdot \vec{B} = 0. \tag{2.3}$$

In fact there are no known magnetic monopoles: magnets always have a north and south pole, and magnetic field lines don't begin at neither of these, but rather loop around and through them (from north to south) or extend to/from infinity, as depicted on Figure 2.2. These two equations are often referred to as the divergence equations.

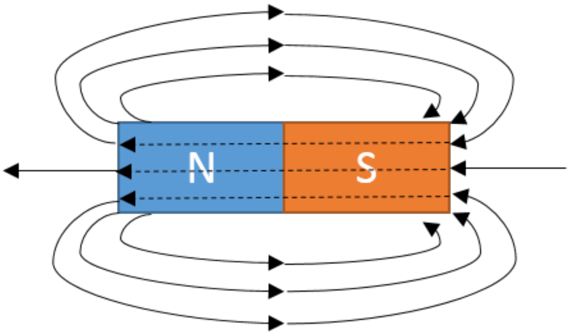

Figure 2.2: Magnetic field lines looping around and inside a magnet.

The other two, commonly called the curl equations, are the induction laws, which give further insight to the origin of these fields and their interaction. Beginning with Faraday's law:

$$\nabla \times \vec{E} = -\frac{\partial \vec{B}}{\partial t}, \tag{2.4}$$

where "$\nabla\times$" is the curl operator. The equation shows how the existence of a time-varying magnetic field generates a spatially varying electric field. To complement this phenomenon, we go to the last of Maxwell's equation, Ampère's law with Maxwell's correction:

$$\nabla \times \vec{H} = \vec{J} + \varepsilon \frac{\partial \vec{E}}{\partial t}. \tag{2.5}$$

In this equation, $\vec{J}$ denotes the free currents present. This shows that both a temporally varying electric field and an electric current can induce a spatially varying magnetic field.

If we look at these two phenomena, we can see that if one field generates another, this generated field, as it goes from zero to its actual value, varies in time. This variation will in turn induce another field – despite no charges or currents being present – and so on. It is this succession of self-inducing electric and magnetic fields that is behind electromagnetic waves, propagating through space. One can in fact (as Maxwell did) deduce the electromagnetic wave equation from this set of four equations. It was from this deduction that the scottish physicist concluded "that light is an electromagnetic disturbance propagated through the field according to electromagnetic laws" in his work *A Dynamic Theory of the Electromagnetic Field*, in 1864 [13].

Our goal is to solve Maxwell's curl equations over a domain that emulates retinal tissue, in order to determine how light scatters when it propagates through it. Analytical solutions for these equations are difficult to obtain and are only available in very simple cases and for problems possessing a great deal of symmetry. For practical situations, analytical methods become mostly useless, which is why the use of numerical methods is so welcome [25]. The finite-difference time-domain method solves the curl equations numerically [17, 25, 26] and will be introduced and explored in the next chapter.

2.4 Wave Propagation

The induction phenomena behind electromagnetic waves propagation are described by Maxwell's equations, as explained above. An electromagnetic wave propagates in space at a speed that depends on the medium's permittivity, ε, and permeability, μ. These quantities, ε and μ, express the measure to which a material is able to support the formation of an electric or a magnetic field, respectively. The speed at which the electromagnetic wave propagates in the medium relates to these quantities by $v = \frac{1}{\sqrt{\mu\varepsilon}}$. Another way to characterise the speed of electromagnetic radiation in a certain medium is through the medium's refractive index, $n = \frac{c}{v}$, where c is the speed of light in vacuum.

When an electromagnetic field is so far from whatever its source is that its behaviour remains unchanged regardless of alterations in the source itself, we refer to it as far field (otherwise, we say its a near field situation). In this way, changes in charges and currents that generate fields affect the near field, and not directly the far field. In these terms, we can call the far field an electromagnetic wave. An electromagnetic wave, or electromagnetic radiation, carries energy through space [13, 15]. This form of energy is transmitted and absorbed by electrically charged particles and exhibits a wave-like behaviour described by the induction phenomena described in the previous section. In fact, one can obtain the electromagnetic wave equation by manipulation of the four equations, (2.2), (2.3), (2.4) and (2.5).

If we take Faraday's law, (2.4), in a medium where no charges or currents are present, and take the curl of both sides, we have

$$\nabla \times (\nabla \times \vec{E}) = \nabla \times \left(-\frac{\partial \vec{B}}{\partial t} \right)$$

and through the curl properties, we get

$$\nabla(\nabla \cdot \vec{E}) - \nabla^2 \vec{E} = -\frac{\partial}{\partial t}(\nabla \times \vec{B}).$$

Using Ampère's Law, (2.5), it yields

$$\nabla^2 \vec{E} = \frac{\partial}{\partial t}\left(\mu_0 \varepsilon_0 \frac{\partial \vec{E}}{\partial t}\right)$$

and then

$$\nabla^2 \vec{E} - \mu_0 \varepsilon_0 \frac{\partial^2}{\partial t^2}\vec{E} = 0,$$

which finally gives us the wave equation,

$$\left(\nabla^2 - \mu_0 \varepsilon_0 \frac{\partial^2}{\partial t^2}\right)\vec{E} = 0.$$

A similar process yields an identical result for the magnetic field.

The fact that electromagnetic fields travel through space as waves allows us to understand a series of phenomena that involve light. Two of them – scattering and interference – are of pivotal importance when it comes to OCT; as such, we will give special focus to both of them.

2.4.1 Scattering

Scattering is the general physical phenomenon where a wave is forced to change its trajectory by inhomogeneities in the medium where it travels. This change in the medium can result in a reflection, a refraction or both.

Refraction occurs as light passes between two media with different refraction indexes. The speed at which light travels is related to the medium's refractive index; as a wave travels between different media, the speed at which it travels changes, but the wave's frequency doesn't. In order to enforce the principle of conservation of energy and momentum the wave bends its path. The relation between the incidence angle, θ_1, the refraction angle, θ_2, and the media's refraction coefficients (n_1 the incidence medium and n_2 the refraction medium) is described by Snell's law:

$$\frac{\sin\theta_1}{\sin\theta_2} = \frac{n_2}{n_1}.$$

In general, the wave is not only refracted but also partially reflected back. In the context of optical coherence tomography, this portion that is back-reflected is the one of interest regarding the output signal. Fresnel's equations give us the fraction of the wave that is refracted, T, transmittance, and the fraction that is reflected, R, reflectance. These relate to each other, due to the conservation of energy, by $T = 1 - R$. For a 90 ° incidence, the reflectance is given by $R = \left|\frac{n_1 - n_2}{n_1 + n_2}\right|^2$. From this we can see clearly how the refractive indexes influence the amount of light that is back-reflected and therefore detected in the OCT apparatus. Since these refractive indexes are characteristic each material, it is clearer how this information can help to identify the structure that reflects the wave. The backscattered portion of the wave is the one that is going to interfere with the reference beam and contribute to the OCT image.

2.4.2 Interference

Interference is one of the most important principles behind OCT. This is related to the fact that electromagnetic fields follow the superposition principle: at a certain point, the net field is the sum of the fields generated by different sources at that point. However, given the oscillatory nature of the electromagnetic wave, at a certain point, fields created by different sources may interfere constructively, i.e., the net result is bigger than the intervening fields, or destructively, when the resulting field is smaller than the original fields. This phenomenon can be simply visualized graphically, on Figure 2.3.

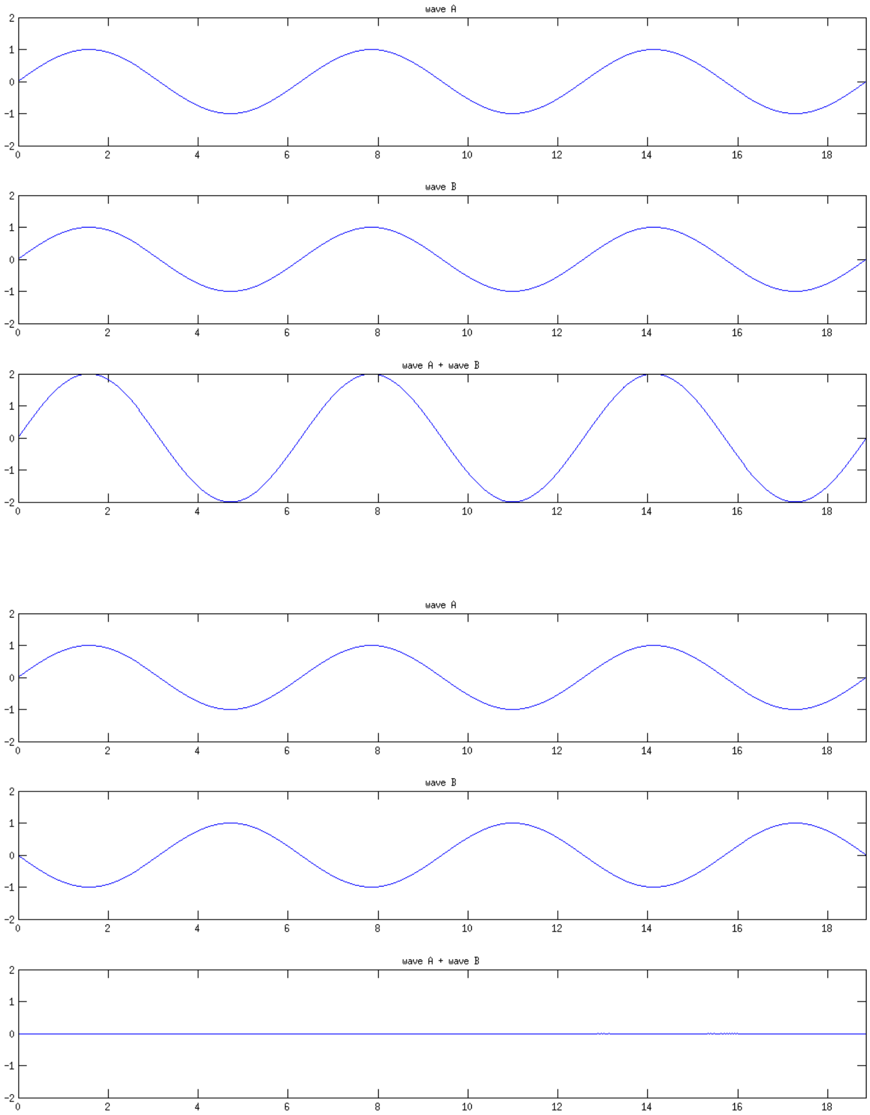

Figure 2.3: Constructive and destructive interference. In both cases, the wave in the third plot is the sum of the waves in the previous two. Note that in the first set of images, the crests and valleys of the waves are aligned and as such they are "maximized" in the resulting wave; in the second set, the crests are aligned with the valleys and they add up to zero.

In OCT, as it was described in the previous chapter, the signal that reaches the detector is the result of two beams interfering with each other. The detector doesn't directly acquire the value of the electric field, but rather the irradiance (the time average of the square of the electric field), for instance. Before further explanation about calculating the irradiance, it should be mentioned that an electromagnetic wave may be expressed in complex form, as $Ae^{i(kx-\omega t)}$ (where A is the amplitude, and k and ω are the wave's number and frequency). Having said this, the relation between the irradiance and the electric field can be described by $I \propto < EE^* >$, where E^* is the complex conjugate of the electric field and $< >$ the time average. The irradiance at the detector is related to the electric field from the sample, E_s, and to the one from the reference arm, E_r, by the following:

$$\begin{aligned} I_D \propto < E_D E_D^* > =& (1/2) < E_r E_r^* > + (1/2) < E_s E_s^* > + \\ & (1/2) < E_r^* E_s > + (1/2) < E_s^* E_r > \end{aligned}$$

a few simplifications lead to:

$$\begin{aligned} I_D \propto < E_D E_D^* > = (1/2) I_R + (1/2) I_S + & (1/2) < E_r^* E_s > + \\ & (1/2) < E_s^* E_r > \end{aligned}$$

where I_R is the irradiance due to the field from the reference arm and I_S from the sample. The last terms can be called the interference terms, and it is them that carry the information needed to build an OCT image [7].

2.5 Model

When building our model, we must start by defining what our domain will be. Our domain is going to emulate a portion of the retina that corresponds to one pixel in the OCT scan; this translates in rectangle with dimensions $5\,\mu m \times 15\,\mu m$. We will then have a rectangular domain, Ω, which is related to the retina as shown in Figure 2.4, (a). On Figure 2.4 (b) we have a better representation of our computational domain; the empty area will be necessary to include our source term, but such details are to be explained ahead.

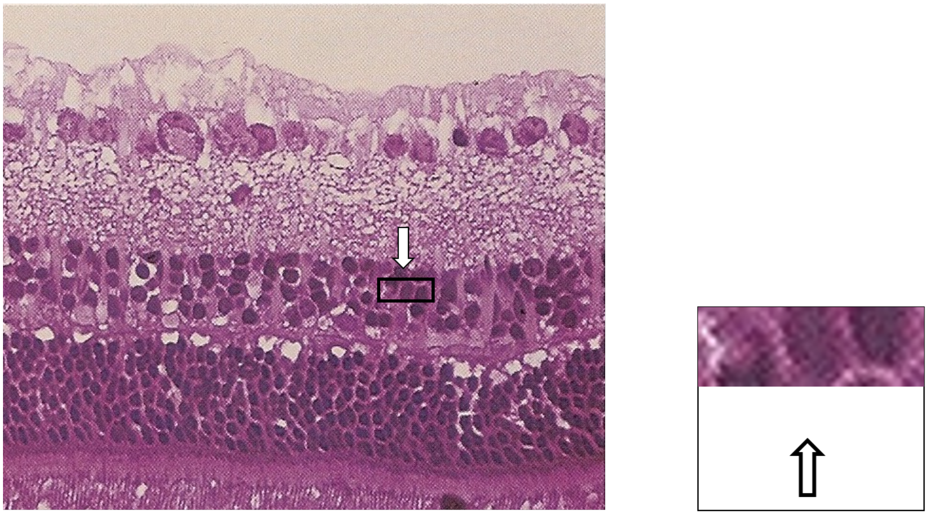

(a) *(b)*

Figure 2.4: (a) Representation of the computational domain; (b) the square limits of the computational domain. The arrow indicates the direction of propagation of light.

If we take Maxwell's curl equations, (2.4) and (2.5), and expand the curls in cartesian coordinates, we get:

$$\frac{\partial \vec{H}}{\partial t} = -\frac{1}{\mu}\nabla \times \vec{E} \Rightarrow \begin{cases} \dfrac{\partial H_x}{\partial t} = -\dfrac{1}{\mu}\left(\dfrac{\partial E_z}{\partial y} - \dfrac{\partial E_y}{\partial z}\right) \\[2ex] \dfrac{\partial H_y}{\partial t} = -\dfrac{1}{\mu}\left(\dfrac{\partial E_x}{\partial z} - \dfrac{\partial E_z}{\partial x}\right) \\[2ex] \dfrac{\partial H_z}{\partial t} = -\dfrac{1}{\mu}\left(\dfrac{\partial E_y}{\partial x} - \dfrac{\partial E_x}{\partial y}\right) \end{cases}$$

and

$$\frac{\partial \vec{E}}{\partial t} = \frac{1}{\varepsilon}\nabla \times \vec{H} \Rightarrow \begin{cases} \dfrac{\partial E_x}{\partial t} = \dfrac{1}{\varepsilon}\left(\dfrac{\partial H_z}{\partial y} - \dfrac{\partial H_y}{\partial z}\right) \\ \dfrac{\partial E_y}{\partial t} = \dfrac{1}{\varepsilon}\left(\dfrac{\partial H_x}{\partial z} - \dfrac{\partial H_z}{\partial x}\right) \\ \dfrac{\partial E_z}{\partial t} = \dfrac{1}{\varepsilon}\left(\dfrac{\partial H_y}{\partial x} - \dfrac{\partial H_x}{\partial y}\right) \end{cases} .$$

Computing all six resulting equations would result in a time consuming process that isn't practical. To avoid this issue, we decompose the fields into two modes: a "transverse electric", TE, and "transverse magnetic", TM [26]. The reduction to any of these modes implies that the wave is uniform in the z-direction, and extends to infinity – and so all the partial derivatives with respect to z are 0. This two modes are characterized in the following way:

1. TE mode:

$$\begin{aligned} H_x &= H_y = 0,\ E_z = 0, \\ \frac{\partial E_x}{\partial t} &= \frac{1}{\varepsilon}\left(\frac{\partial H_z}{\partial y}\right), \\ \frac{\partial E_y}{\partial t} &= \frac{1}{\varepsilon}\left(\frac{\partial H_z}{\partial x}\right), \\ \frac{\partial H_z}{\partial t} &= -\frac{1}{\mu}\left(\frac{\partial E_y}{\partial x} - \frac{\partial E_x}{\partial y}\right). \end{aligned} \tag{2.6}$$

2. TM mode:

$$\begin{aligned} H_z &= 0,\ E_x = E_y = 0, \\ \frac{\partial E_z}{\partial t} &= \frac{1}{\varepsilon}\left(\frac{\partial H_y}{\partial x} - \frac{\partial H_x}{\partial y}\right), \\ \frac{\partial H_x}{\partial t} &= -\frac{1}{\mu}\left(\frac{\partial E_z}{\partial y}\right), \\ \frac{\partial H_y}{\partial t} &= -\frac{1}{\mu}\left(\frac{\partial E_z}{\partial x}\right). \end{aligned}$$

In this way, we can solve for only one of the modes and still have an accurate portrayal of reality [25]. With this, we have reduced the number of equations we have to solve by half without compromising our results. Our model will then consist of the transverse electric mode equations for the electromagnetic fields, (2.6).

To complement our model, we need to consider boundary and initial conditions. As visible on Figure 2.4, our area of interest isn't physically bounded in the real case; as such, artificial boundary conditions that mimic a lack of physical boundary will be necessary. In the next chapter different options will be discussed. As for initial conditions, our fields' initial values will be zero, except for H_z, where we will start with a term that will act as a source for the electromagnetic wave:

$$\begin{aligned} E_x(x,y,0) &= 0; \\ E_y(x,y,0) &= 0; \\ H_z(x,y,0) &= F(x,y,0). \end{aligned} \tag{2.7}$$

In this work we will consider the function F as the gaussian function with amplitude A, centred in the point $(x_0, y_0) \in \Omega$ and scale parameters σ_x and σ_y that represent the spreads of the curve along the s an y directions. We take in consideration that its width must be small enough that its value on the borders of our domain is zero, as depicted on Figure 2.5.

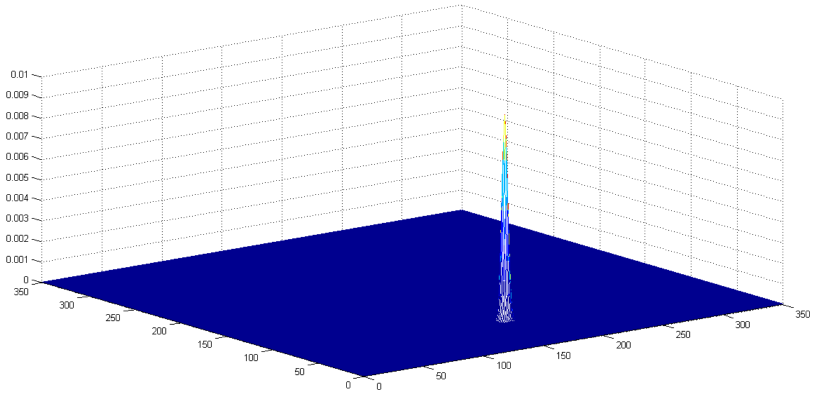

Figure 2.5: Gaussian curve in our computational domain; $A = 0.005$, $(x_0, y_0) = (75, 175)$ (in a domain $\Omega = [0, 350] \times [0, 350]$), and $\sigma_x = \sigma_y = 2$.

Chapter 3

Numerical Method

3.1 State of the Art

The finite differences method has been used to calculate the numerical solution of Maxwell's equations for many years. In 1966, Kane Yee published a paper [26] where he described the numerical basis for solving Maxwell's curl equations (Faraday's and Ampère's law) directly in time, in a spatial domain. However, despite the simplicity of the method, its computational charge and storage costs were considerable for the computers of those days; only later, in the late seventies/eighties, was the method more generally applied. The term "finite difference time domain" (FDTD) was coined by Taflove in 1980, in a paper where he published the first validated models of a sinusoidal wave propagating in a tridimensional cavity. In 1977, Engquist and Majda developed absorbing boundary conditions (ABC) for numerical simulations of waves [11], and the finite difference scheme for those boundary conditions was developed by Mur in 1981 [21]. In 1988, Kriegsmann *et al.* and Moore *et al.* published the first papers on ABC theory. In 1994, Berenger published a paper introducing the highly effective perfectly matched layer (PML) boundary conditions [4] for bidimensional domains; in the same year, Katz *et al.* extended these boundary conditions for tridimensional domains. From then on, there have been numerous improvements to this numerical method, including an alternating-direction implicit (ADI) FDTD algorithm, proven to be unconditionally numerically stable [25].

3.2 Finite Difference Time Domain

The exact solution for Maxwell's curl equations is very hard to determine, and this is why the use of numerical methods is so welcome. The finite-difference time-domain method solves the curl equations numerically. One of the most important parts of this method, constructed by Kane Yee in 1966 [26], is the development of an appropriate spatial grid. Since we will work in a bi-dimensional domain, we will focus on this type of domains. It should be said that this method is also of possible application for tridimensional domains. The particularity of Yee's grid is that rather than being computed at the same point, there are specific points in which we compute each field component, arranged between themselves as illustrated on Figure 3.1.

Let $\Omega = [0, X] \times [0, Y]$, $\Delta x = \frac{X}{N_x}$, $\Delta y = \frac{Y}{N_y}$, N_x, N_y positive integers. We define the subsets:

$$\begin{aligned}
\Omega_1 &= \{(i\Delta x, j\Delta y) \in \Omega,\ i = 0, \dots, N_x, j = 0, \dots, N_y\};\\
\Omega_2 &= \{((i+1/2)\Delta x, j\Delta y) \in \Omega,\ i = 0, \dots, N_x - 1, j = 0, \dots, N_y\};\\
\Omega_3 &= \{(i\Delta x, (j+1/2)\Delta y) \in \Omega,\ i = 0, \dots, N_x, j = 0, \dots, N_y - 1\}.
\end{aligned}$$

Following the nomenclature above, Ω_1 includes the points where H_z is computed, Ω_2 is where E_y is computed, and Ω_3 is where E_x is computed. Since our spatial domain is to mimic the retina, specifically at a cellular level, we must choose a spatial step small enough.

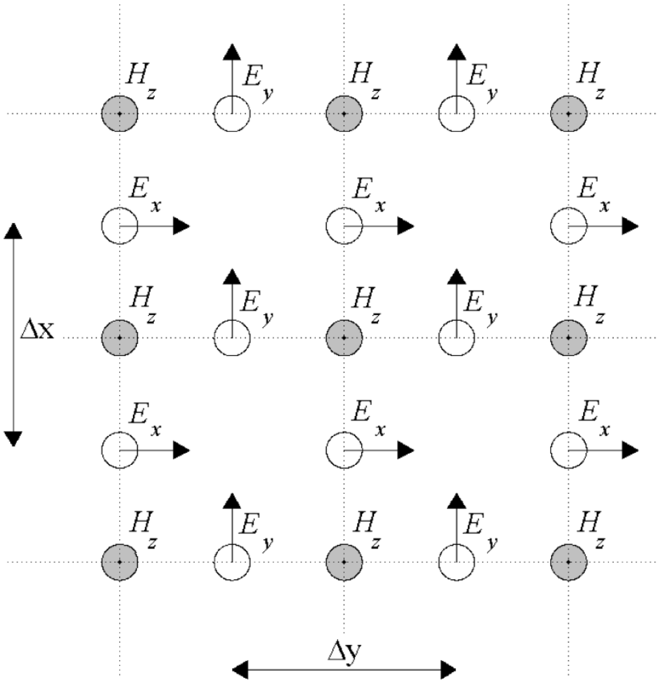

Figure 3.1: Scheme of the spatial grid for the TE mode.

Also, it is said in the literature [25] that in these simulations, at least 10 samples per wavelength should be taken. Since in OCT $\lambda = 10^{-6}m$, and for the dimensions we're aiming for, we choose $\Delta x = \Delta y = \Delta s = 10^{-7}m$. Temporally, we will run our simulation from $t = 0$ until $t = T_{final}$, with intermediate values $t^n = n\Delta t$, where $\Delta t = \frac{T_{final}}{N_t}$, $n = 0, \ldots, N_t$ and N_t a positive integer.

By choosing the spatial step, we impose a certain upper limit on the possibilities of our time step; following the Courant-Friedrichs-Lewy (CFL) stability condition [10, 25]:

$$\Delta t \leq \frac{C\Delta s}{2c},$$

where C is the CFL stability factor, which for this method, following the literature, is $C = \frac{1}{\sqrt{2}}$. This condition imposes that the maximum possible value for Δt is $1.178511301977579^{-16}\,s$, a value that despite being so small allows for the stable computation of the electric field values.

Having our choice of time and spatial steps, we must now set up our equations over the grid previously defined. We take the TE equations, (2.6), and set them in our grid:

$$
\begin{aligned}
\frac{\partial E_x}{\partial t}(i\Delta s,(j+1/2)\Delta s,(n+1/2)\Delta t) &= \frac{1}{\varepsilon(i\Delta s,(j+1/2)\Delta s)} \\
&\left(\frac{\partial H_z}{\partial y}(i\Delta s,(j+1/2)\Delta s,(n+1/2)\Delta t)\right), \\
\frac{\partial E_y}{\partial t}((i+1/2)\Delta s,j\Delta s,(n+1/2)\Delta t) &= \frac{1}{\varepsilon((i+1/2)\Delta s,j\Delta s)} \\
&\left(\frac{\partial H_z}{\partial x}((i+1/2)\Delta s,j\Delta s,(n+1/2)\Delta t)\right), \\
\frac{\partial H_z}{\partial t}(i\Delta s,j\Delta s,n\Delta t) = -\frac{1}{\mu(i\Delta s,j\Delta s)} &\left(\frac{\partial E_y}{\partial x}(i\Delta s,j\Delta s,n\Delta t)-\right. \\
&\left.\frac{\partial E_x}{\partial y}(i\Delta s,j\Delta s,n\Delta t)\right).
\end{aligned}
$$

Next, we discretize our set of equations using central differences as follows:

$$
\begin{aligned}
&\frac{E_x(i\Delta s,(j+1/2)\Delta s,(n+1)\Delta t)-E_x(i\Delta s,(j+1/2)\Delta s,n\Delta t)}{\Delta t} = \\
&\frac{1}{\varepsilon(i\Delta s,(j+1/2)\Delta s)}\left(\frac{H_z(i\Delta s,(j+1)\Delta s,(n+1/2)\Delta t)}{\Delta s}-\right. \\
&\left.\frac{H_z(i\Delta s,j\Delta s,(n+1/2)\Delta t)}{\Delta s}\right)+O(\Delta s^2)+O(\Delta t^2);
\end{aligned}
$$

$$\frac{E_y((i+1/2)\Delta s, j\Delta s, (n+1)\Delta t) - E_y((i+1/2)\Delta s, j\Delta s, n\Delta t)}{\Delta t} =$$
$$\frac{1}{\varepsilon((i+1/2)\Delta s, j\Delta s)} \left(\frac{H_z((i+1)\Delta s, j\Delta s, (n+1/2)\Delta t)}{\Delta s} - \right.$$
$$\left. \frac{H_z(i\Delta s, j\Delta s, (n+1/2)\Delta t)}{\Delta s} \right) + O(\Delta s^2) + O(\Delta t^2);$$

$$\frac{H_z(i\Delta s, j\Delta s, (n+1/2)\Delta t) - H_z(i\Delta s, j\Delta s, (n-1/2)\Delta t)}{\Delta t} =$$
$$\frac{1}{\mu(i\Delta s, j\Delta s)} \left(\frac{E_y((i+1/2)\Delta s, j\Delta s, n\Delta t)}{\Delta s} - \right.$$
$$\frac{E_y((i-1/2)\Delta s, j\Delta s, n\Delta t)}{\Delta s} - \frac{E_x(i\Delta s, (j+1/2)\Delta s, n\Delta t)\Delta s}{\Delta s} -$$
$$\left. \frac{E_x(i\Delta s, (j-1/2)\Delta s, n\Delta t)}{\Delta s} \right) + O(\Delta s^2) + O(\Delta t^2).$$

At this point, we introduce the notation $H_{z(i,j)}^{n+1/2}$ for the approximation of the z component of the magnetic field at the point $(i\Delta s, j\Delta s)$ of our grid at the instant $(n+1/2)\Delta t$, $E_{x(i,j+1/2)}^{n}$ for the approximation of the x component of the electric field at the point $(i\Delta s, (j+1/2)\Delta s)$, $E_{y(i+1/2,j)}^{n}$ for the approximation of the y component of the electric field at the point $((i+1/2)\Delta s, j\Delta s)$, at the instant $n\Delta t$. This way, we get the set of equations:

$$\begin{cases} \dfrac{H^{n+1/2}_{z(i,j)} - H^{n-1/2}_{z(i,j)}}{\Delta t} & = -\dfrac{1}{\mu_{(i,j)}} \left(\dfrac{E^{n}_{y(i+1/2,j)} - E^{n}_{y(i-1/2,j)}}{\Delta s} \right. \\ & \qquad \left. - \dfrac{E^{n}_{x(i,j+1/2)} - E^{n}_{x(i,j-1/2)}}{\Delta s} \right), \\ \dfrac{E^{n+1}_{x(i,j+1/2)} - E^{n}_{x(i,j+1/2)}}{\Delta t} & = \dfrac{1}{\varepsilon_{(i,j+1/2)}} \left(\dfrac{H^{n+1/2}_{z(i,j+1)} - H^{n+1/2}_{z(i,j)}}{\Delta s} \right), \\ \dfrac{E^{n+1}_{y(i+1/2,j)} - E^{n}_{y(i+1/2,j)}}{\Delta t} & = -\dfrac{1}{\varepsilon_{(i+1/2,j)}} \left(-\dfrac{H^{n+1/2}_{z(i+1,j)} - H^{n+1/2}_{z(i,j)}}{\Delta s} \right). \end{cases} \tag{3.1}$$

And so we have the field update equations to be used when solving the electromagnetic field values as described in the Yee algorithm. There are several things that make this algorithm a robust choice for dealing with these kind of problems. First, the fact that it solves both the electric and the magnetic field in time and space, rather than solving either one of the fields individually using a wave equation. Second, the grid in itself is constructed in such a way that illustrates Faraday's and Ampère's laws: the fact that each field component is surrounded by the field components that influence it, makes it simpler to identify the components associated with displacement currents or magnetic fluxes, and implicitly enforces Gauss's laws, (2.2) and (2.3), (as the mesh is divergence-free).

3.3 Initial Conditions

Our initial conditions, described in the previous chapter, will translate into initial values for $H^{-1/2}_{z(i,j)}$ and for $E^{0}_{x(i+1/2,j)}$ and $E^{0}_{y(i,j+1/2)}$. In (2.7), $F(x,y)$ can be any kind of impulse. We will use a gaussian impulse, such as

$$F(x,y) = Ae^{-\frac{(x-x_0)^2}{2\sigma_x^2} - \frac{(y-y_0)^2}{2\sigma_y^2}}$$

where A is the amplitude, (x_0, y_0) is the center of the gaussian and σ_x and σ_y are the spread of the curve along the x and y directions, respectively. In our specific case, we will have $A = 0.005$, $(x_0, y_0) = (75, 175)$ (in a domain $\Omega = [0, 350] \times [0, 350]$), and $\sigma_x = \sigma_y = 2$. This is graphically shown in Figure 3.2.

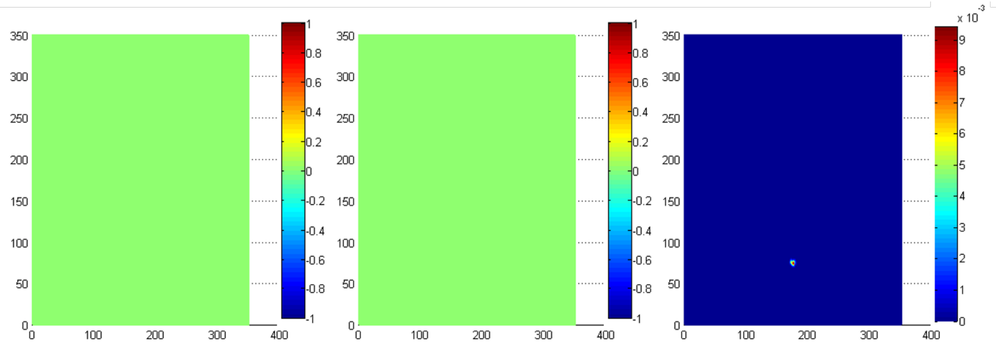

(a) *(b)* *(c)*

Figure 3.2: Initial Conditions. (a) shows E_x, (b) shows E_y and (c) shows H_z.

Note that at the boundaries, all the fields are equal to 0.

3.4 Boundary Conditions

For wave propagation simulations, there is always the boundary condition issue. In the real case, an electromagnetic wave keeps propagating until it eventually dies off, or is absorbed by a certain obstacle. Simulating a domain large enough for the wave to die off by itself would be far too computationally heavy and of no interest; as such, we need to choose an appropriate boundary condition in order to simulate the real life situation.

3.4.1 Dirichlet Boundary Condition

The Dirichlet boundary conditions are of no use to solve the problem presented above, but a mention to them is necessary as they are sort of our base for comparisons. As seen in the previous section, the value of all the fields ate the boundaries will initially be 0. Since the field update equations need values for the electric/magnetic field above/below/right/left of the cell in which we are calculating the field (which value is needed depends on the field being calculated), the electromagnetic fields at the borders won't be updated. This means that at the borders, the value of the fields is always zero. This value, despite not being updated, is needed in order to update the fields in the adjacent cells; since it is always 0, it will interfere with the fields inside the domain, causing a reflection effect (which can be seen in the Numerical Results chapter ahead on Figures 4.4, 4.5 and 4.6). It is to prevent this unwanted reflection that we will need an appropriate boundary condition.

3.4.2 Mur's Absorbing Boundary Condition

In 1977, Engquist and Majda proposed a theoretical boundary condition that would absorb outgoing waves at the border of the computational domain [11]. In short, we would have what would be equivalent to a one-way wave equation that, when applied at the outer boundaries of the domain, absorbs outgoing waves. If we define the partial differential operator

$$G \equiv \frac{\partial^2}{\partial x^2} + \frac{\partial^2}{\partial y^2} - \frac{1}{c^2}\frac{\partial^2}{\partial t^2},$$

we can write the bidimensional wave equation, $\frac{\partial^2 U}{\partial x^2} + \frac{\partial^2 U}{\partial y^2} - \frac{1}{c^2}\frac{\partial^2 U}{\partial t^2} = 0$, simply as $GU = 0$. We can factorize this operator as follows:

$$G^+ \equiv \frac{\partial}{\partial x} + \frac{\partial}{\partial t}\frac{1}{c}\sqrt{1 - \frac{\frac{\partial}{\partial y}}{\frac{\partial}{\partial t}c}}, \qquad G^- \equiv \frac{\partial}{\partial x} - \frac{\partial}{\partial t}\frac{1}{c}\sqrt{1 - \frac{\frac{\partial}{\partial y}}{\frac{\partial}{\partial t}c}},$$

where

$$G = G^{+}G^{-}.$$

Engquist and Majda showed that if we apply G^{-} at the left boundary, it will absorb an outgoing plane wave in that direction. However, this term includes a square root, making this a "pseudo-differential" operator. It was in 1981 that Mur showed how one can approximate this square root to different orders so that the boundary condition can be implemented [21]. The approximations, however, are not exact, and some amount of reflection can occur as the waves cross the boundary; this effect can be minimised while designing the boundary condition by, for instance, increasing the order to which the square root approximation is exact.

The second order absorbing boundary condition (ABC) for a domain with dimensions $[0, X] \times [0, Y]$ is as follows:

$$\begin{array}{lll}
\dfrac{\partial^2 U}{\partial x \partial t} - \dfrac{1}{c}\dfrac{\partial^2 U}{\partial t^2} + \dfrac{c}{2}\dfrac{\partial^2 U}{\partial y^2} = 0 & \text{for} & x = 0, y \in [0, Y] \\
\dfrac{\partial^2 U}{\partial x \partial t} + \dfrac{1}{c}\dfrac{\partial^2 U}{\partial t^2} - \dfrac{c}{2}\dfrac{\partial^2 U}{\partial y^2} = 0 & \text{for} & x = X, y \in [0, Y] \\
\dfrac{\partial^2 U}{\partial y \partial t} - \dfrac{1}{c}\dfrac{\partial^2 U}{\partial t^2} + \dfrac{c}{2}\dfrac{\partial^2 U}{\partial x^2} = 0 & \text{for} & x \in [0, X], y = 0 \\
\dfrac{\partial^2 U}{\partial y \partial t} + \dfrac{1}{c}\dfrac{\partial^2 U}{\partial t^2} - \dfrac{c}{2}\dfrac{\partial^2 U}{\partial x^2} = 0 & \text{for} & x \in [0, X], y = Y
\end{array}$$

3.4.3 Perfectly Matched Layer

The perfectly matched layer (PML) boundary condition is considered state of the art in these type of works. It was originally proposed by Bérenger in 1994 [4]. Essentially, a PML is a lossy layer in which electromagnetic waves are absorbed gradually; this is achieved by surrounding our domain of interest with a region where there is a certain value of what can be called conductivity, even though it is more of a numerical construct to have the absorption effect we're looking for, that causes the wave to be absorbed gradually. This term enters our equations (2.4) and (2.5) associated with the free currents term and with an equivalent term for the magnetic case, the equivalent magnetic current density, that despite having no physical realization, has numerical interest for this study. These "currents" can act as independent sources of energy for the electric and magnetic fields, as $\sigma\vec{E}$ and $\sigma^*\vec{H}$. This way, the curl equations become:

$$\begin{aligned} \nabla \times \vec{E} &= -\mu\frac{\partial \vec{H}}{\partial t} - (\sigma^*\vec{H}), \\ \nabla \times \vec{H} &= \varepsilon\frac{\partial \vec{E}}{\partial t} + (\sigma\vec{E}). \end{aligned} \tag{3.2}$$

If we give a certain value to σ and σ^* in a layer that surrounds our domain, and make them zero in our area of interest, we will have created a lossy layer that absorbs outgoing waves. However, for obliquely incident waves, this formulation doesn't quite work, leaving a certain amount of reflection behind. To address this issue, Bérenger proposed what is called a *split field formulation* – he split the equation that governs the evolution of H_z in two, as follows:

$$\frac{\partial H_z}{\partial t} = -\frac{1}{\mu}\left(\left(\frac{\partial E_y}{\partial x} - \frac{\partial E_x}{\partial y}\right) - \sigma^* H_z\right)$$

is split in

$$\frac{\partial H_{zx}}{\partial t} = -\frac{1}{\mu}\left(\frac{\partial E_y}{\partial x} - \sigma_x^* H_z\right)$$

and

$$\frac{\partial H_{zy}}{\partial t} = -\frac{1}{\mu}\left(-\frac{\partial E_x}{\partial y} - \sigma_y^* H_z\right).$$

In this way, we can write $H_z = H_{zx} + H_{zy}$. Now, using the modified curl equations and the split-field formulation for H_z, we get the following field update equations:

$$\begin{aligned}
H^{n+1/2}_{zx(i,j)} &= \frac{\mu_{(i,j)} - 0.5\Delta t\sigma^*_x}{\mu_{(i,j)} + 0.5\Delta t\sigma^*_x} H^n_{zx(i,j)} \\
&+ \frac{\Delta t}{\Delta s(\mu_{(i,j)} + 0.5\Delta t\sigma^*_x)}(-E^n_{x(i,j+1/2)} + E^n_{x(i,j-1/2)}),
\end{aligned}$$

$$\begin{aligned}
H^{n+1/2}_{zy(i,j)} &= \frac{\mu_{(i,j)} - 0.5\Delta t\sigma^*_y}{\mu_{(i,j)} + 0.5\Delta t\sigma^*_y} H^n_{zy(i,j)} \\
&+ \frac{\Delta t}{\Delta s(\mu_{(i,j)} + 0.5\Delta t\sigma^*_y)}(E^n_{y(i+1/2,j)} - E^n_{y(i-1/2,j)}),
\end{aligned}$$

$$\begin{aligned}
E^{n+1}_{x(i,j+1/2)} &= \frac{\varepsilon_{(i,j)} - 0.5\Delta t\sigma_x}{\varepsilon_{(i,j)} + 0.5\Delta t\sigma_x} E^n_{x(i,j+1/2)} \\
&+ \frac{\Delta t}{\Delta s(\varepsilon_{(i,j)} - 0.5\Delta t\sigma_x)}(H^{n+1/2}_{z(i,j+1)} - H^{n+1/2}_{z(i,j)}),
\end{aligned}$$

$$\begin{aligned}
E^{n+1}_{y(i+1/2,j)} &= \frac{\varepsilon_{(i,j)} - 0.5\Delta t\sigma_y}{\varepsilon_{(i,j)} + 0.5\Delta t\sigma_y} E^n_{y(i+1/2,j)} \\
&- \frac{\Delta t}{\Delta s(\varepsilon_{(i,j)} - 0.5\Delta t\sigma_y)}(H^{n+1/2}_{z(i+1,j)} - H^{n+1/2}_{z(i,j)}).
\end{aligned}$$

The indexes x and y in the conductivity and magnetic loss constants refer not to the field components, but to propagation direction. Looking at the final set of equations, we see we have all our fields in these two directions, which are normal to the interface between the lossy layer and the domain of interest; as such, the unwanted reflections are avoided.

Another consideration is that this lossy layer has to be *perfectly matched* with our domain of interest, or else undesired reflections may occur when the wave goes from one to the other. In a medium with a certain constant permittivity and permeability, if $\sigma = \sigma_x = \sigma_y$, $\sigma^* = \sigma_x^* = \sigma_y^*$, and if these values are related by $\sigma^* = \sigma \frac{\mu}{\varepsilon}$, we have an absorbing medium that is impedance-matched to our domain of interest [22, 25].

Chapter 4

Numerical Results

Before introducing the results obtained, some considerations that were needed regarding implementation will be mentioned. First, if we look at equations (3.1), we note that many of the indexes have half-integer values; this comes from the staggered mesh arrangement previously described. When implementing the equations, such indexes aren't possible; because of this, we will slightly change our equations in a way that all the indexes are integers - quite simply we just change our reference point, in such a way that the index ±1/2 when respecting to the magnetic field update equations, becomes 1 or 0, and when respecting to the electric field update equations becomes 0 or -1. This translates a simple change in referential that makes implementation a lot simpler. We now present the field update equations, ready for implementation:

$$
\begin{aligned}
H^{n+1}_{z(i,j)} &= H^{n}_{z(i,j)} + \frac{\Delta t}{\Delta s \mu_{(i,j)}}(E^{n}_{y(i,j)} - E^{n}_{y(i-1,j)} - E^{n}_{x(i,j)} + E^{n}_{x(i,j-1)}),\\
E^{n+1}_{x(i,j)} &= E^{n}_{x(i,j)} + \frac{\Delta t}{\Delta s \varepsilon_{(i,j)}}(H^{n+1}_{z(i,j+1)} - H^{n+1}_{z(i,j)}),\\
E^{n+1}_{y(i,j)} &= E^{n}_{y(i,j)} - \frac{\Delta t}{\Delta s \varepsilon_{(i,j)}}(H^{n+1}_{z(i+1,j)} - H^{n+1}_{z(i,j)}).
\end{aligned}
$$

It is important to emphasize that despite the points having the same indexes, the logic behind the staggered meshes is maintained and that this change is purely for implementation simplicity.

We will first simulate the temporal evolution of the electromagnetic fields over the domain $\Omega = [0, 350] \times [0, 350]$, where at every point $\varepsilon = \varepsilon_0$, with initial conditions

$$\begin{aligned} E_x(x, y, 0) &= 0; \\ E_y(x, y, 0) &= 0; \\ H_z(x, y, 0) &= 0.005 e^{-\frac{(x-175)^2}{8} - \frac{(y-175)^2}{8}}. \end{aligned}$$

The result of this simulation is presented in Figures 4.1, 4.2 and 4.3.

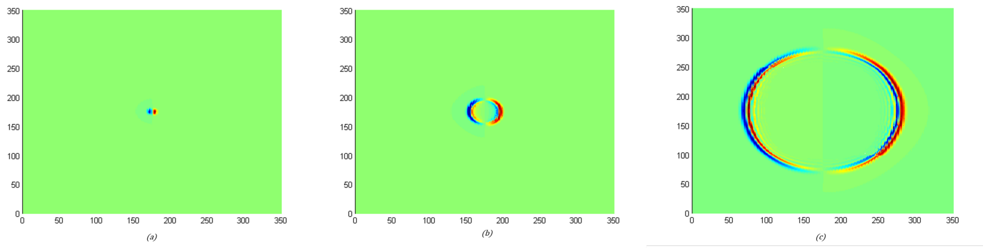

Figure 4.1: Temporal evolution of E_x. (a) $t = 10\Delta t$; (b) $t = 60\Delta t$; (c) $t = 300\Delta t$.

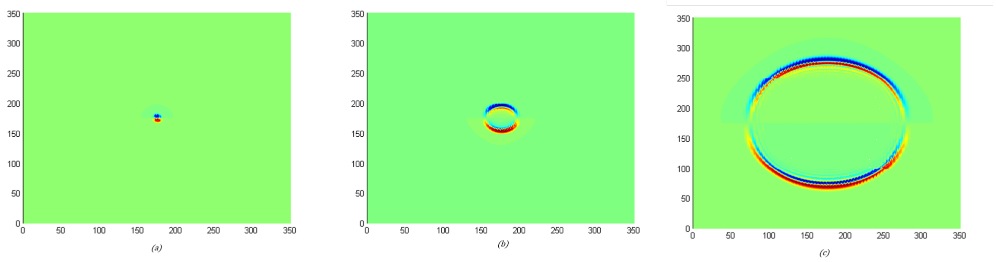

Figure 4.2: Temporal evolution of E_y. (a) $t = 10\Delta t$; (b) $t = 60\Delta t$; (c) $t = 300\Delta t$.

As we can see, the mechanism of induction causes the fields to propagate spherically across our domain. At approximately $t = 500\Delta t$, the wave reaches the borders of our domain. Our "default"

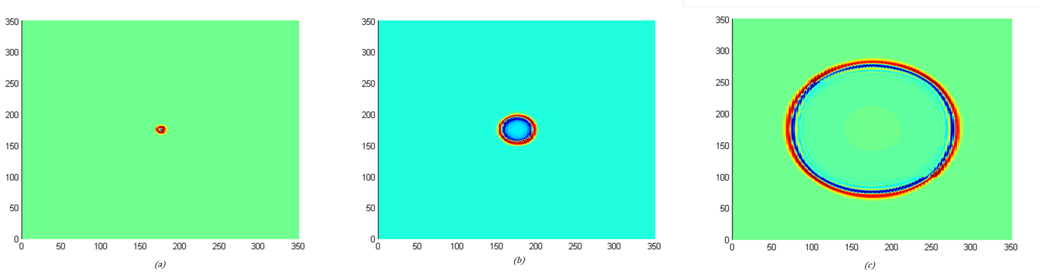

Figure 4.3: Temporal evolution of H_z. (a) $t = 10\Delta t$; (b) $t = 60\Delta t$; (c) $t = 300\Delta t$.

boundary conditions, as explained previously, are Dirichlet boundary conditions. In Figures 4.4, 4.5 and 4.6 we see the effect this boundary condition has on our fields.

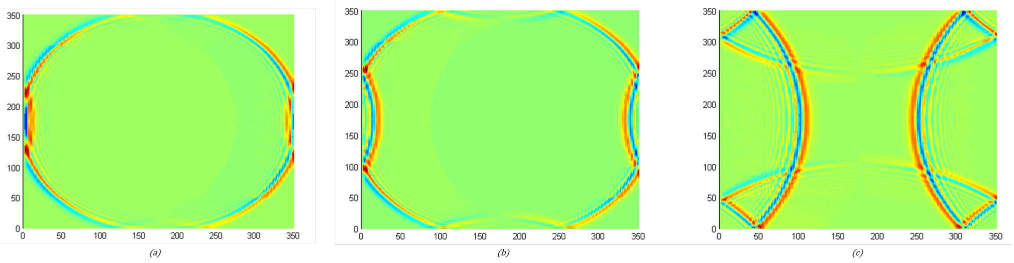

Figure 4.4: Temporal evolution of E_x. (a) $t = 520\Delta t$; (b) $t = 550\Delta t$; (c) $t = 800\Delta t$.

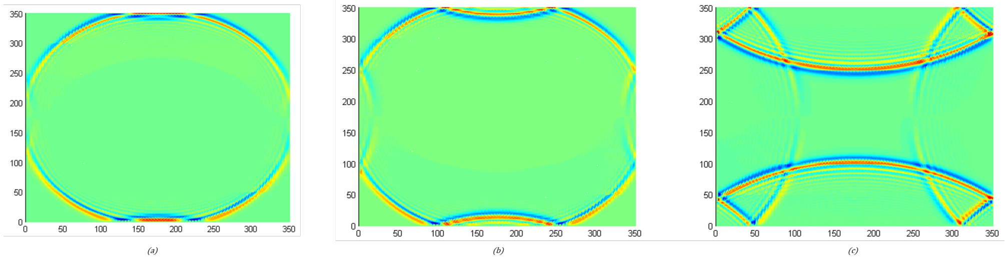

Figure 4.5: Temporal evolution of E_y. (a) $t = 520\Delta t$; (b) $t = 550\Delta t$; (c) $t = 800\Delta t$.

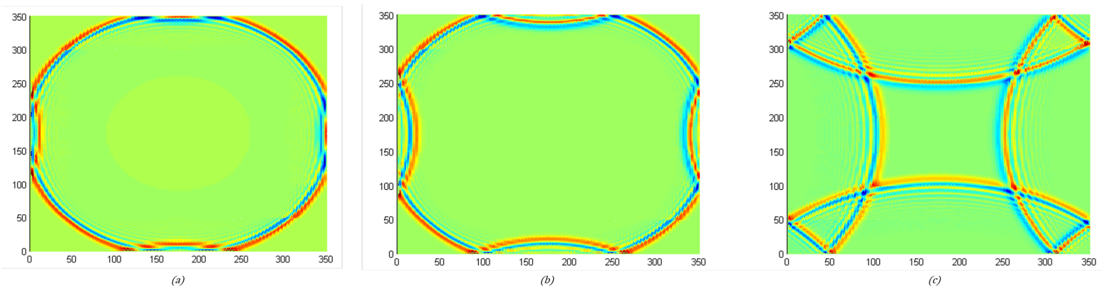

(a) (b) (c)

Figure 4.6: Temporal evolution of H_z. (a) $t = 520\Delta t$; (b) $t = 550\Delta t$; (c) $t = 800\Delta t$.

In the previous figures, the reflection effect that the Dirichlet boundary conditions have is quite clear.

Following these results, we present now the obtained field components when we run a simulation with the same initial conditions but with Mur's second order ABC in Figure 4.7.

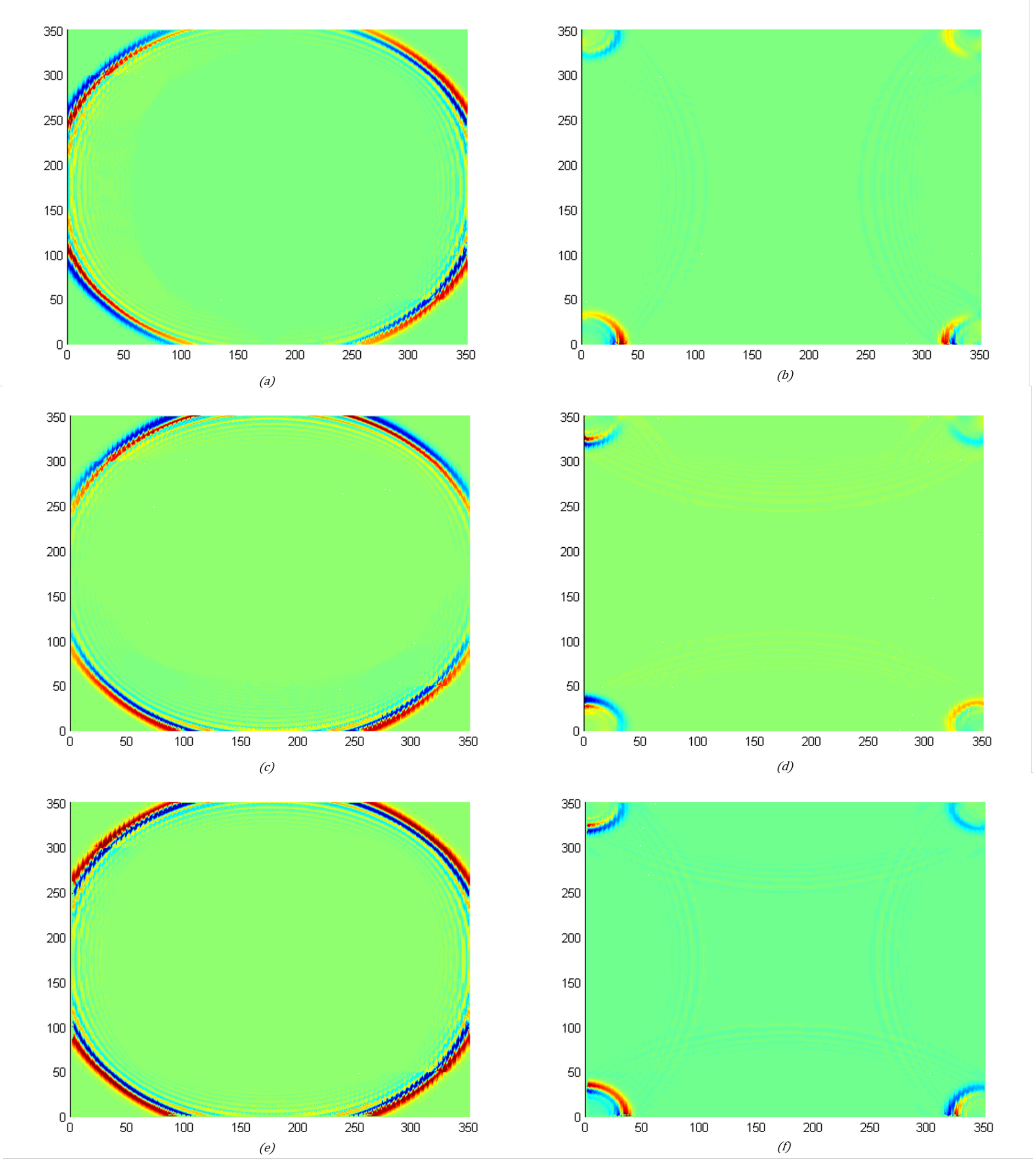

Figure 4.7: Temporal evolution of E_x, E_y and H_z. (a) and (b) show E_x at instants $t = 550\Delta t$ and $t = 800\Delta t$, respectively; (c) and (d) show E_y, and (e) and (f) show H_z, for the same instants as the first two.

It is clear when comparing Figure 4.4 (e) and (f) with Figure 4.7 (a) and (b) that most of the field is absorbed at the boundary (equivalent remarks can be made between the other field components). It is also clear that at the corners there are artefacts that would require further care. However, in this work, we preferred implementing the PML boundary condition rather than further improving Mur's ABC. Before showing the results for this boundary, a brief mention to the choice of values for $\sigma_x, \sigma_y, \sigma_x^*$ and σ_y^* will be made.

There are several examples in the literature of ways of choosing gradually crescent values for the conductivity and magnetic loss. For our work, we chose to do an adaptation of the code provided by Dr. Susan Hagness [25]. In Figure 4.8 we present our obtained results for a PML that is 50 cells wide.

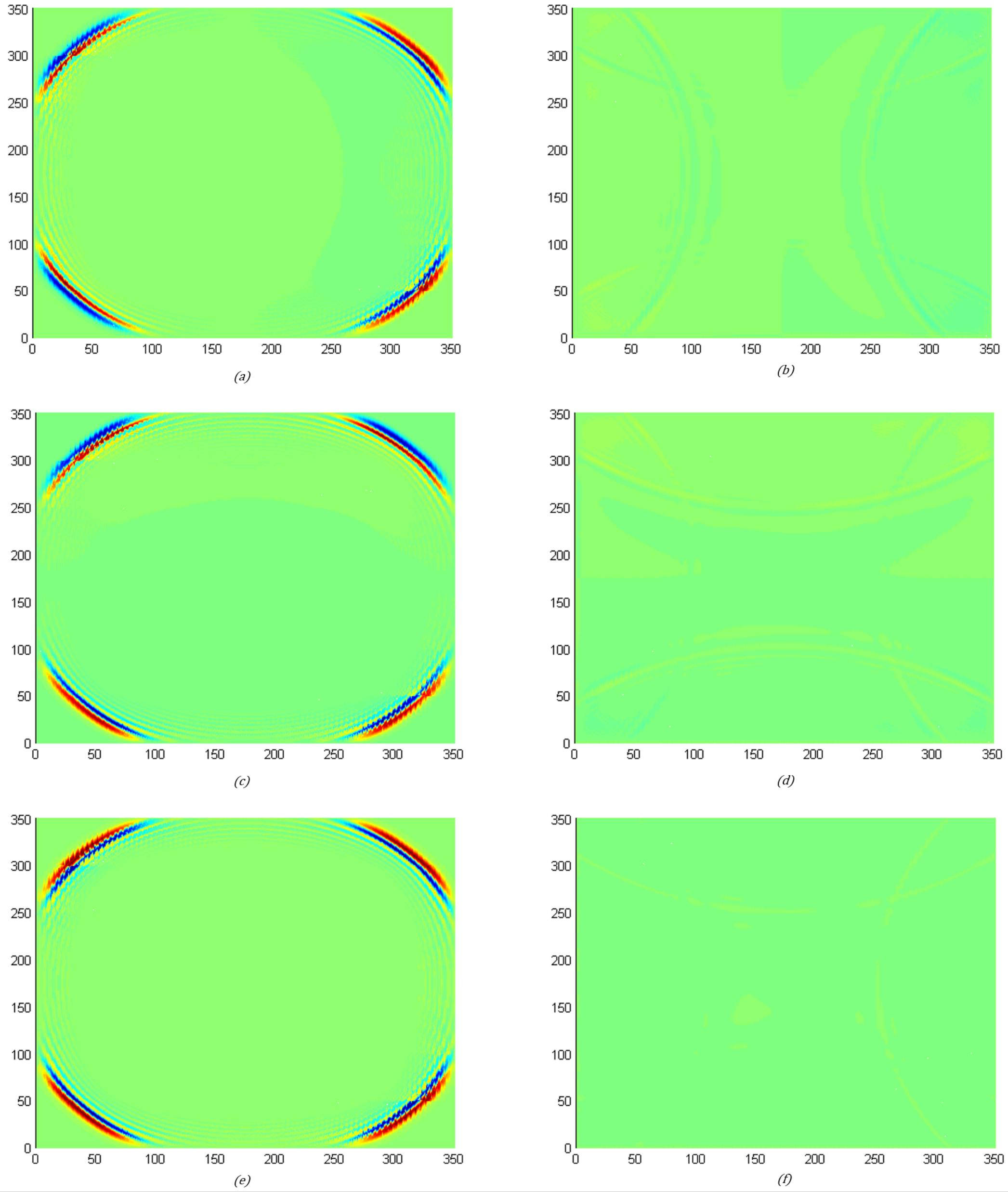

(a) (b)

(c) (d)

(e) (f)

Figure 4.8: Temporal evolution of E_x, E_y and H_z. (a) and (b) show E_x at instants $t = 550\Delta t$ and $t = 800\Delta t$, respectively; (c) and (d) show E_y, and (e) and (f) show H_z, for the same instants as the first two.

Comparing with Figures 4.4, 4.5 and 4.6, it is obvious how much more effective this boundary condition is in preventing undesired reflections at the borders. If we compare, image by image, Figures 4.7 and 4.8, we see that in (a), (c) and (d), in the PML case the absorption is more evident at this instant, and in (b), (d) and (f), we can see that in the PML case there are no artefacts in the corners and the fields are practically zero at this instant. This lead us to the decision, which is supported by the literature [4, 25], that the PML boundary condition serves our purposes on this work better than Mur's ABC, and as such we will use it for further simulations.

We will now introduce a change in the medium's permittivity ε, in order to observe the reflection and refraction effects that were described in a previous chapter. This way, our domain will look like the scheme on Figure 4.9.

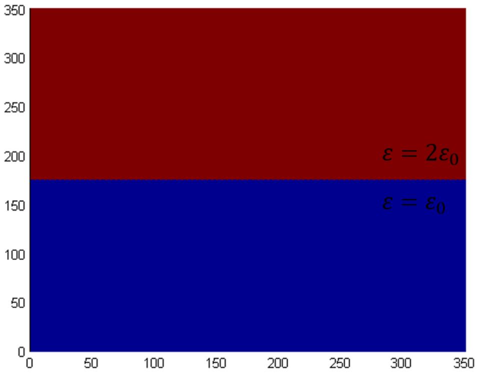

Figure 4.9: Domain for the single interface simulation. Note the values for ε: $\varepsilon = 2\varepsilon_o$ (top); $\varepsilon = \varepsilon_o$ (bottom).

In order to have our source factor farther away from the interface our initial conditions will also slightly change to:

$$\begin{aligned} E_x(x,y,0) &= 0; \\ E_y(x,y,0) &= 0; \\ H_z(x,y,0) &= 0.005e^{-\frac{(x-175)^2}{8}-\frac{(y-75)^2}{8}}. \end{aligned}$$

This way, when our electromagnetic wave reaches our area of interest, it has approximately a plane wave shape.

For boundary condition we will use a PML identical to the one described above. From now on, rather than plotting the values of the fields, we will plot the intensity of the wave, calculated as $I = \sqrt{E_x^2 + E_y^2}$, which is our approximation to the irradiance mentioned in a previous chapter.

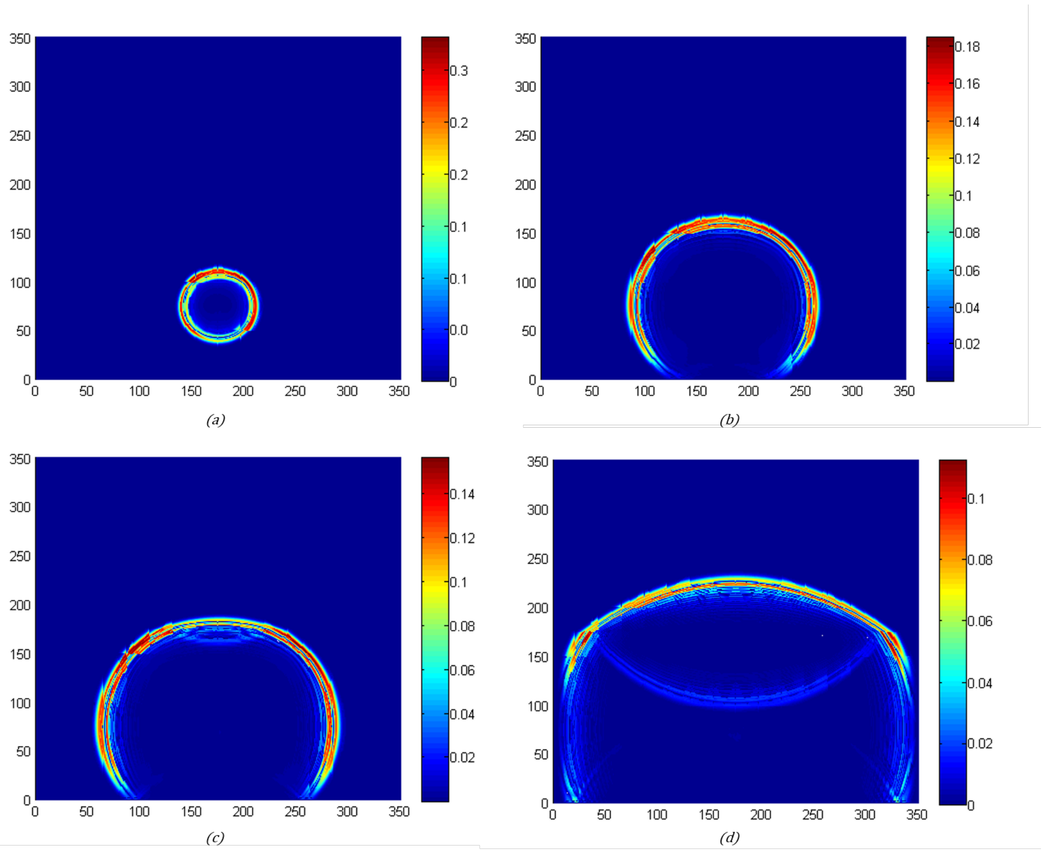

(a) (b) (c) (d)

Figure 4.10: Evolution of the intensity of the wave over a single interface (a) $t = 100\Delta t$; (b) $t = 250\Delta t$; (c) $t = 320\Delta t$; (d) $t = 500\Delta t$.

In Figure 4.10, we can see clearly a part of the beam transmitted through the interface, with a slightly bent trajectory compared to the one in the first medium, and a part that is back-reflected.

In order to get closer to our initial goal of simulating the evolution of the fields over a domain that mimics a section of the retina that corresponds to an OCT scan, we now move on to a domain where we have a single cell where $\varepsilon = 1.8769\varepsilon_0$, which is approximately the value of permittivity in the INL of mice [9]. Besides this change, we will also change the width of our PML layer; rather than being 50 cells wide all around the domain, it will be as depicted on Figure 4.11.

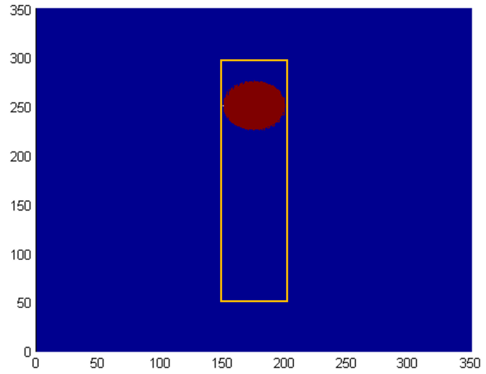

Figure 4.11: Domain for the single cell simulation.

The PML region is outside the yellow rectangle. Our initial conditions will be the same as in the previous example.

We can see on Figure 4.12 (d) the two reflections that correspond to the two interfaces that the wave passes through. These back-reflections will be what the OCT apparatus detects in order to build the final image.

For our final simulation, we will have a domain that aims to mimic Figure 2.4. In this simulation, the initial conditions are the same as in the previous simulations. The source factor is far away from our domain of interest so that when the wave reaches the cells, its configuration is nearly plane (hence the empty area depicted on Figure 2.4). The results are shown in Figure 4.14.

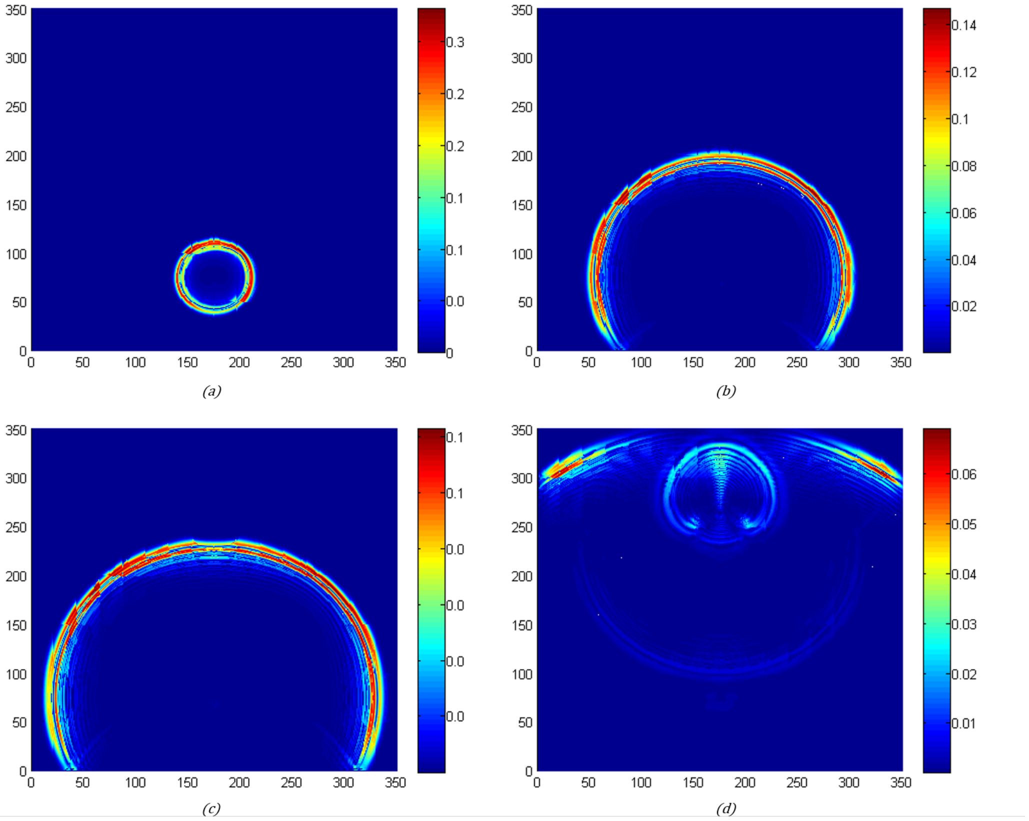

Figure 4.12: Simulation with a single cell. Plot of the intensity at different instants: (a) $t = 100\Delta t$; (b) $t = 350\Delta t$; (c) $t = 550\Delta t$; (d) $t = 800\Delta t$.

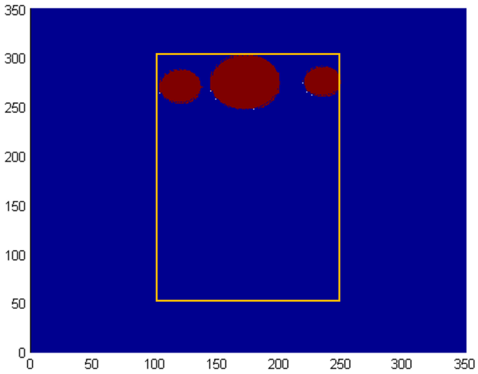

Figure 4.13: Domain for the OCT pixel simulation.

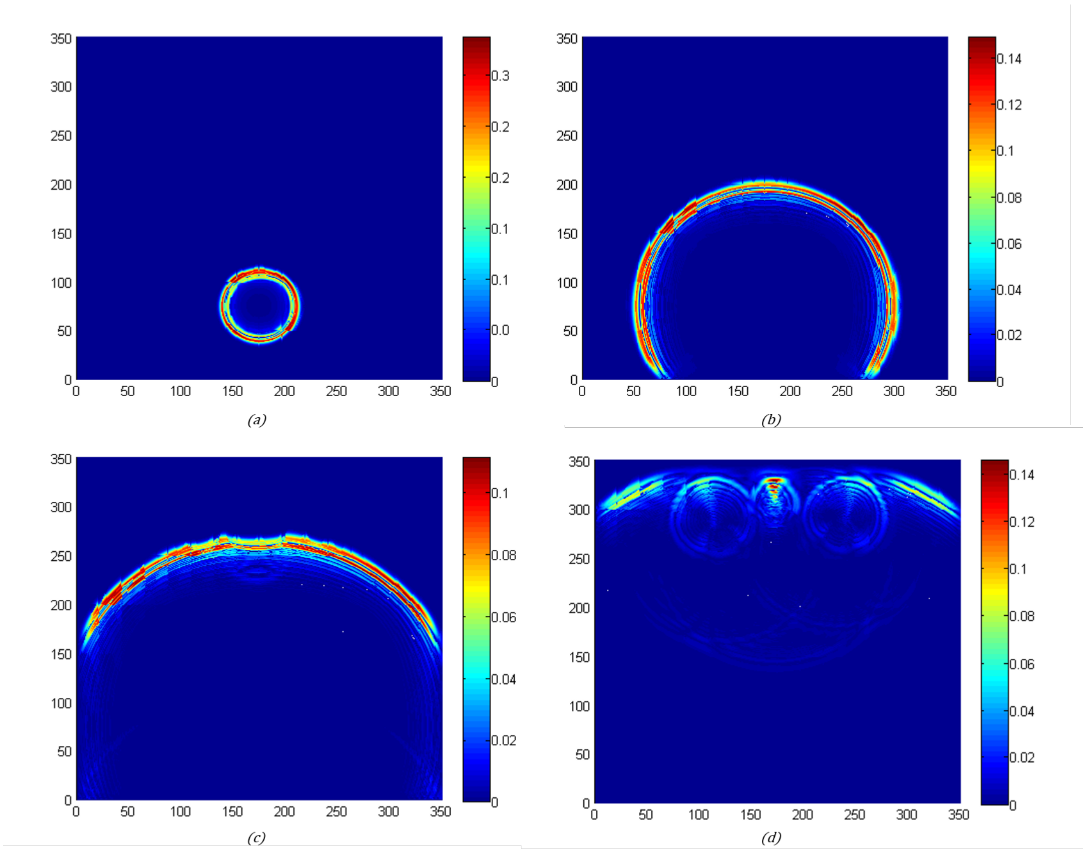

Figure 4.14: Simulation in an OCT pixel. Plot of the intensity at different instants: (a) $t = 100\Delta t$; (b) $t = 350\Delta t$; (c) $t = 550\Delta t$; (d) $t = 800\Delta t$.

Note that in Figure 4.14 (d) we can see the back-reflections that correspond to each cell. This signal is detected by the photodetector in the OCT apparatus, and will correspond to one pixel in the OCT scan. Our research group, at AIBILI, is working with other numerical methods that have different strengths compared with FDTD. A discontinuous Galerkin, DG , method has been used frequently [3]. In order to cross-validate the results obtained with FDTD and with DG, we ran a simulation for the same domain and with the same boundary and initial conditions. In Figure 4.15 we present the obtained results.

The clear similarities between Figures 4.15 and 4.14 encourage our

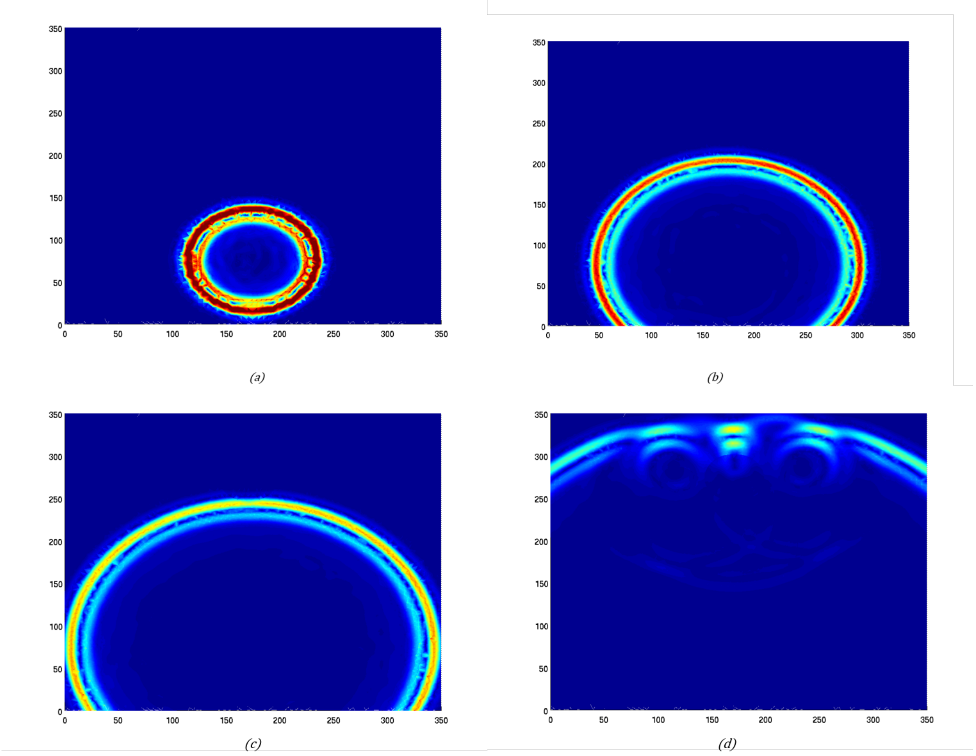

(a) (b) (c) (d)

Figure 4.15: Simulation in an OCT pixel with DG. Plot of the intensity at different instants: (a), $t = 100\Delta t$; (b), $t = 350\Delta t$; (c), $t = 550\Delta t$; (d), $t = 800\Delta t$.

belief that our model provides accurate results for this problem.

Chapter 5

Conclusions and Future Work

In this work, we have successfully described a mathematical model for light scattering problems that is based on Maxwell's equations. We have also described a domain analogous to the equivalent of an OCT pixel in the retina. The results obtained with FDTD and with the DG method are coherent between each other; this works as some sort of validation for both methods. A more in-depth study into the correlation between the results can be useful for futher studies. However, by visual inspection alone, we can say that both methods give identical results. We can, through statistical methods, build the equivalent results for a complete layer and even a full OCT scan.

This is one of the future works for our research group. To validate the results obtained in this way, we will need to run simulations (with FDTD or DG) over the complete layer; this is another task for us in the near future.

Bibliography

[1] S. Abdallah, O. Ramahi, and K. Bizheva. FDTD Simulation of Electromagnetic Wave Scattering from Retina Cells. In *IEEE Eng Med Biol Soc2*, pages 1639–1642, 2007.

[2] E. Alarousu. *Low coherence interferometry and optical coherence tomography in paper measurements.* PhD thesis, University of Oulu, 2006.

[3] Adérito Araújo, Sílvia Barbeiro, Luís Pinto, Francisco Caramelo, António L. Correia, Miguel Morgado, Pedro Serranho, Ana Sílvia F. C. Silva, and Rui Bernardes. No Title. In *International Conference on Computational and Mathematical Methods in Science and Engineering*, pages 121–129, 2013.

[4] Jean-Pierre Berenger. A perfectly matched layer for the absorption of electromagnetic waves. *Journal of Computational Physics*, 114(2):185–200, October 1994.

[5] Rui Bernardes, José Cunha-Vaz, and Pedro Serranho. *Optical Coherence Tomography: a Concept Review.* Biological and Medical Physics, Biomedical Engineering. Springer Berlin Heidelberg, Berlin, Heidelberg, 2012.

[6] B. E. Bouma and G. J. Tearney. *Handbook of optical coherence tomography.* Marcel Dekker, 2002.

[7] Mark E. Brezinski. *Optical Coherence Tomography: Principles and Applications.* Academic Press, 2006.

[8] N. Bulow. Light Scattering by pigment epithelium granules in the Human retina. *Acta Ophtalmol*, 46:1048–1053, 1968.

[9] Enping Chen. Refractive Indices of the Rat Retinal Layers. *Ophtalmic Res*, 25:65–68, 1993.

[10] NEVA Electromagnetics. A 3D FDTD code implemented in MATLAB, 2011.

[11] Bjorn Engquist and Andrew Majda. Absorbing Boundary Condition for the Numerical Simulation of Waves. *Mathematics of Computation*, 31(139):629–651, 1977.

[12] A. F. Fercher, W. Drexler, C. K. Hitzenberger, and T. Lasser. Optical coherence tomography — principles and applications. 66:239–303, 2003.

[13] Richard P. Feynman. *The Feynman Lectures on Physics.* Addison–Wesley, 2 edition, 1964.

[14] James G. Fujimoto. Optical coherence tomography. *Comptes Rendus de l'Académie des Sciences - Series IV - Physics*, 2(8):1099–1111, October 2001.

[15] David J. Griffiths. *Introduction to Electrodynamics.* 1999.

[16] H. Hammer, D. Schweitzer, E. Thamm, A. Kolb, and J. Strobel. Scattering properties of the retina and the choroids determined from OCT-A-Scans. *International Ophthalmology*, 23:291–295, 2001.

[17] R. Horváth. Finite Difference Solution of Maxwell's Equations. In *Application of Numerical Analysis in Computational Science*, chapter 1. 2004.

[18] David Hubel. *Eye, Brain, and Vision.* Harvard Medical (Online).

[19] Frederik A. Jakobiec. *Ocular Anatomy Embryology and Teratology*. Harper & Row, 1982.

[20] Luiz Junqueira and Jose Carneiro. *Basic Histology: Text & Atlas (Junqueira's Basic Histology)*. McGraw-Hill Medical, 2005.

[21] Gerrit Mur. Absorbing Boundary Conditions for the Finite-Difference Approximation of the Time-Domain Electromagnetic-Field Equations. *IEEE Transactions on Electromagnetic Compatibility*, EMC-23(4):377–382, 1981.

[22] John B. Schneider. Understanding the Finite-Difference Time-Domain Method, 2010.

[23] K. Si, W. Gong, and C. Sheppard. Model for light scattering in biological tissue and cells based on random rough nonspherical particles. *Appl Opt*, 48:1153–1157, 2009.

[24] Ana Sílvia F. C. Silva and António L. Correia. From optical coherence tomography to Maxwell's equations. *IEEE 3rd Portuguese Meeting in Bioengineering*, pages 1–4, 2013.

[25] Allen Taflove and Susan C. Hagness. *Computational Electrodynamics*. Artech House, 2 edition, 2000.

[26] Kane S. Yee. Numerical solution of initial boundary value problems involving Maxwell's equations in isotropic media. *Antennas and Propagation, IEEE Transactions on*, AP-14, no.:302–307, 1966.

Index